UNIVERSITÀ DEGLI STUDI DI PADOVA

Dipartimento di Fisica e Astronomia "Galileo Galilei"

Corso di Laurea Magistrale in Fisica

Tesi di Laurea

Variational theory of confinement effects

on cholesteric liquid crystals

Relatore

Prof. Enzo Orlandini

Correlatori

Prof. Raffaele Mezzenga

Dr. Salvatore Assenza

Laureando

Paride Azzari

Anno Accademico 2017/2018

in collaboration with

ETH *zürich*

Department of Health Sciences and Technology

Institute of Food, Nutrition and Health

Laboratory of Food and Soft Materials

Acknowledgements

Introduction

The discovery and the first theories of liquid crystals came out at the beginning of the last century, however they became materials of growing importance from the 60s. For these last 60 years, the research regarding liquid crystals required both science and technology to work together, especially with the advent of liquid crystals displays.

Nowadays researchers are looking for new applications of liquid crystals knowledge to new materials and biological structures. Particularly, interest has grown for *chiral* liquid crystals, also known as *cholesteric* liquid crystals. The presence of chirality has always fascinated scientists, since understanding and controlling chirality brings many challenges and has many implications as shown in [1].

In this work, we address theoretically the effects of confinement on chiral liquid crystals. Recent experimental works on cholesteric droplets based on amyloid fibrils [2] found that these droplets undergo three different phase transitions at growing volumes, changing their shape. These four phases are called: *homogenous, bipolar, uniaxial cholesteric* and *onion*.

The complete phenomenology has, to date, not yet been described or predicted from a theoretical perspective in a unique model. Simple scaling arguments based on bulk terms of the Frank-Oseen (FO) energy-density functional have been derived by Van Der Shoot [3] and Mezzenga [2] only for the first three phases, namely: homogeneous, bipolar and cholesteric. To rationalize the full spectrum a more thorough analysis is needed. In this work, we will address the issue by means of a variational approach, with particular focus on understanding how confinement affects the various terms of the FO functional, for both bulk and surface terms.

In Chapter 1, we briefly review the phenomenology and properties of liquid crystals, including birefringence, with a short introduction of Jones matrices. In Chapter 2 the experimental system is present, with a focus on the experimental data that is used to develop the theory. The classical continuum theory of liquid crystal is reviewed in Chapter 3, where a functional for bulk liquid crystals is introduced. The case of free boundary is discussed in Chapter 4, where the full free energy functional is showed. In the following chapters three models are presented to rationalize the system of Chapter 2. The first model (Chapter 5) is able to describe only part of the tactoids, namely the homoge-

nous to bipolar transition. The second model (Chapter 6) is introduced as a tool to better understand the effect of cholesteric liquid crystals under confinement. The last model, in Chapter 7, is able to describe the full phenomenology showed in Chapter 2, although with some inaccuracies. In the last Chapter, conclusions are drawn and possible future developments are discussed.

Contents

1. Liquid Crystals

In this chapter we briefly introduce liquid crystals, following [4] and [5]. We shortly introduce their phenomenology and properties, with a focus on their birefringency. The last paragraphs describe how to simulate the outcome of polarized optical microscopy on liquid crystals, using Jones calculus.

1.1 Liquid crystals

The term *liquid crystal* (LC) refers to an intermediate state of matter, often referred as a *mesomorphic phase*, that is in between solid crystals and liquid fluids. One of the differences between fluids and crystals lies in the positional order: while in crystals the molecules are located in a periodic lattice, in fluids there is no long-range order. Liquid crystals have an anisotropic order, that means long-range order in only some of the degrees of freedom. This usually reflects a marked shape anisotropy at the molecular level. If we introduce another degree of freedom other than the position, the first candidate is going to be the average direction of the molecule. Long-range order of the direction gives the so called *nematic phase*, while a two-dimensional order gives the *smectic phase*. These categories were introduced by Friedel in 1922 [6], however in this manuscript we are not going to deal with smectic phases. Detailed informations about smectic phases can be found in [4] or [5].

Most of liquid crystals are usually organic substances composed of rod-like molecules, that exhibit liquid crystals phases in two ways: by changing the temperature or by changing the concentration. The former are usually referred as *thermotropic* liquid crystals while the latter are referred as *lyotropic*.

1.2 Nematics

As mentioned above, nematic liquid crystals usually are made of rod-like molecules, with a typical lenght $a \sim 1\,\mathrm{nm}$, usually endowed with a *head-to-tail* symmetry. The most typical molecules that form nematic phases are PAA and MBBA (Figure 1.1).
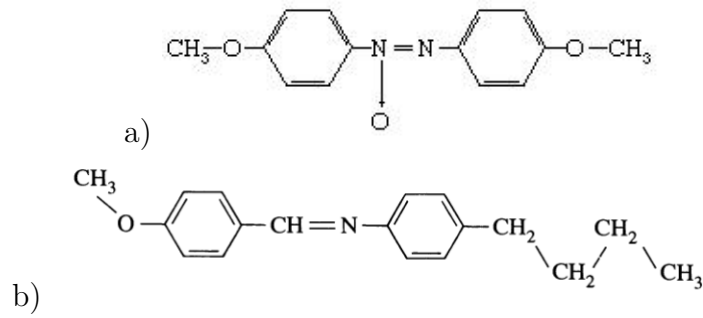
**Figure 1.1:** (a) The PAA molecule is a rigid rod of lenght 2 nm and width 0.5 nm; (b) The MBBA molecule, of similar dimensions.

In the absence of external fields or orienting interactions, the molecules of a nematic liquid crystal acquire a natural orientation, in which their axes are nearly parallel. This natural orientation is usually represented as a unit vector n. Every direction has the same probability to be chosen as a natural orientation. This symmetry is usually reflected in the macroscopic properties of the material, while it is assumed that there is a complete rotational symmetry around n.
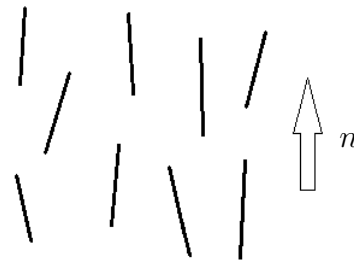
However the vector n should be interpreted as the average orientation of the molecules, not the real direction they lie parallel to. Sometimes the vector n is also called *orientation* or *director*. The vector n may also not be constant throughout the medium,

When the orientational order is completely lost, no direction is privileged and the substance becomes isotropic. For termotropics liquid crystals it happens at a precise temperature, called *clearing temperature*. Analogously, for lyotropics liquid crystals the order is lost at a precise concentration. The temperature ranges for the appearance of a nematic phase are 21°C to 41° C for PAA, and 118°C to 135°C for MBBA [4].

1.3   Cholesterics

A different kind of nematic liquid crystals are the *cholesterics liquid crystals*, or also *chiral nematics.*

Differently from nematics, in the cholesteric bulk phase the vector n is not constant in space. Molecules belonging to the same plane tend to arrange

themselves parallel to each other, but their vector n rotates as one progresses along the axis orthogonal to the plane. To be more specific, given a (x, y, z) reference system where the z-direction is parallel to the cholesteric axis, we have

$$
\begin{aligned}
n_x &= \cos(q_\infty z + \phi_0), \\
n_y &= \sin(q_\infty z + \phi_0), \\
n_z &= 0.
\end{aligned}
\tag{1.1}
$$

where the scalar q_∞ is called the *natural twist* and ϕ_0 is a phase angle, which depends only on the choice of the reference system. Often the twist is represented as a length, called *natural pitch*

$$
p_\infty = \frac{2\pi}{q_\infty}
\tag{1.2}
$$

Due to the head-to-tail symmetry, the structure is periodic along z with a periodicity given by $p_\infty/2$. A typical value of p_∞ is in the order of micrometers, much larger than the dimension of the molecules. Both the sign of q_∞ and its magnitude are important. The sign distinguishes left-handed and right-handed cholesteric, while the magnitude gives the size of the pitch, which is strongly dependent on concentration, temperature, pressure and other variables, see [4] for details.
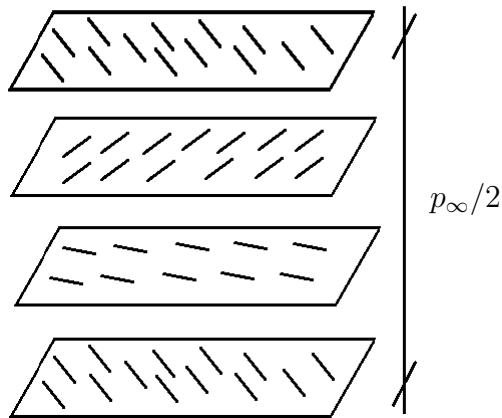
Cholesteric molecules are often helical springs with right or left handedness. Therefore they are not invariant under parity transformations.

1.4 Optical properties of liquid crystals

Liquid crystals constituents are usually strongly anisotropic molecules, thus in their ordered phase, they show optical activity, the most notable example being provided by birefringence [7].

While in optically isotropic materials polarized light can travel without any change of its polarization state, in liquid crystals this is not true anymore since they are optically uniaxial materials, whose optic axis may vary in space. In a uniaxial material there exist two indexes of refraction n_e, n_o called respectively *extraordinary* and *ordinary* indexes. Other optical principles will not be recalled here, an introduction to birefringent materials can be found in [8]. In [9] the authors report that for PAA we have

$$n_o = 1.565, \qquad n_e = 1.829; \tag{1.3}$$

and for MBBA

$$n_o = 1.54, \qquad n_e = 1.75, \tag{1.4}$$

at the wavelength of visible light. In [7] it is is shown that other molecules, which display liquid crystal phases, have closer indexes of refraction with $n_e - n_o \sim 10^{-1} - 10^{-4}$. For instance, carbon-nanotubes in nematic phase have a difference in the indexes of refraction of $0.6 \cdot 10^{-4}$ [3].

One of the typical effects given by the birefringency of nematic liquid crystals are the so called *Schlieren*'s pattern, as the one in Figure 1.2.
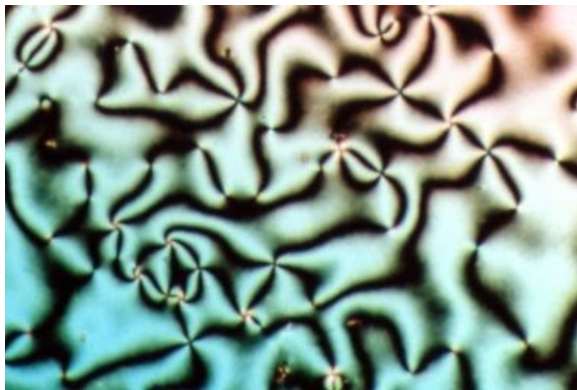
Figure 1.2: Schlieren's texture, taken from [10].

1.5   Jones matrices

In this section we want to briefly describe the Jones calculus, developed by R. C. Jones in [11], used to describe polarized light and the effect that optically active material has on it. A more in-depth discussion can be found in [12]. In a Cartesian space xyz, a polarized plan wave propagating along z can be described as an oscillating vector, with components

$$E_x = E_{0x} \cos\left(\omega\left(t - \frac{z}{c}\right) + \delta_x\right) \tag{1.5}$$

$$E_y = E_{0y} \sin\left(\omega\left(t - \frac{z}{c}\right) + \delta_y\right) \tag{1.6}$$

where $E_{0x,0y}$ are the amplitudes, ω the angular frequency, c the speed of light, and $\delta_{x,y}$ the phases. If we define $\Delta := \delta_y - \delta_x$ we can write a two-dimensional vector E, such that

$$E = \begin{pmatrix} E_{0x} \\ E_{0y}e^{i\Delta} \end{pmatrix} \exp i\left(\omega\left(t - \frac{z}{c}\right) + \delta_x\right) \tag{1.7}$$

where $E_x = \mathrm{Re}(E \cdot e_x)$ and $E_y = \mathrm{Re}(E \cdot e_y)$. The vector E, is referred as a *Maxwell column*. If $\Delta = 0$ the light is *linearly polarized*, if $\Delta = \pi/2$ the light is *circularly polarized*, otherwise the light will be *elliptically polarized*.

The intensity of the light, given the corresponding Maxwell column, is given by the square of complex norm of E:

$$I = E^* \cdot E = E_{0x}^2 + E_{0y}^2 \tag{1.8}$$

In case of a normalized Maxwell column, i. e. $I = 1$, we can represent it as follows

$$E = \begin{pmatrix} \cos(\phi) \\ \sin(\phi)e^{i\Delta} \end{pmatrix} \tag{1.9}$$

The idea behind Jones calculus is that any type of device that acts on polarized light, from polaroid sheets to rotators and pass-planes, can be represented as a 2×2 complex matrix J. This matrix acts on a Maxwell column E_1, which represents the ingoing light, and returns another Maxwell column E_2, the outgoing light. In symbols it can be written as

$$E_2 = JE_1 \tag{1.10}$$

By using the associative property of matrices, the effect of multiple devices can be obtained by multiplying, in the correct order, the matrices of the single devices.

$$E_3 = J_2 E_2 = J_2 J_1 E_1 = JE_1 \tag{1.11}$$

where $J = J_2 J_1$.

Liquid crystals act as linear retarders, in case of the fast axis directed along the x-axis we get

$$J = \begin{pmatrix} 1 & 0 \\ 0 & e^{-i\Lambda} \end{pmatrix} \tag{1.12}$$

where $\Lambda = 2\pi\frac{L}{\lambda}(n_e - n_o)$, λ the wavelength of the light, and L the depth of the liquid crystal sample. Let R be the rotation matrix of angle ϕ, in the xy-plane

$$R(\phi) = \begin{pmatrix} \cos(\phi) & -\sin(\phi) \\ \sin(\phi) & \cos(\phi) \end{pmatrix} \tag{1.13}$$

If n is orthogonal to the direction of the light, that is n is on the xy-plane, then for every angle ϕ that n forms with the x axis, we can write:

$$J(\phi) = R(-\phi)JR(\phi) \tag{1.14}$$

.

1.6   Extended Jones matrix

Since the liquid crystals director is not always constrained on a two-dimensional plane, the Jones matrix method described above is not enough. In the case of liquid crystals, where $n_e \approx n_o$, it is possible to extend the Jones matrix calculus to oblique incidence. The proof and an application to liquid crystals display can be found in [13]. Let θ be the angle of incidence between n and the direction of light. We define

$$n_{eff} := \frac{n_e}{\sqrt{n_o^2 + (n_e^2 - n_o)^2 \cos^2 \theta}} \tag{1.15}$$

and

$$\Lambda = 2\pi \frac{L}{\lambda} n_o. \tag{1.16}$$

The extended Jones' matrix is

$$J = R(-\phi) \begin{pmatrix} e^{i\Lambda n_{eff}} & 0 \\ 0 & e^{i\Lambda} \end{pmatrix} R(\phi) \tag{1.17}$$

where ϕ is the angle between the x axis and the projection of n on the xy-plane.

1.7   Polarized light microscopy simulations

Polarized light microscopy is an optical microscopy technique involving polarized light and used to study birefringent samples. The functioning principle will be recalled here shortly, for more details see [14]. The microscope is equipped with two polarizers, the first called *polarizer* (P) and the second *analyzer* (A), orthogonal to the first. The image is formed by interaction of the light polarized by P with a birefringent sample. When the light of the image passes through the analyzer, the background light is cut out. The resulting image shows only the interaction between the sample and the polarized light.

Using the mathematical method of Jones matrices we want to be able to simulate the result of polarized light microscopy on a sample of given n and given shape. For a constant nematic field n, n_{eff} and ϕ that define (1.17) are constant through the sample and an analytical result can be found. The Jones' matrix of the device can be written as

$$J = J_A J_{\text{sample}} J_P \tag{1.18}$$

where J_A, J_P are the matrices of the polarizer and analyzer, while J_{sample} is the Jones matrix of the whole sample.

In case of a non constant nematic field n, we use numerical simulations to compute the result. In a Cartesian frame x, y, z, where the light travels along z, and the polarizers are parallel to the xy-plane, we discretize the sample in

rectangular cells of step ds much smaller than the length of the sample. We associate to each cell x, y, z a Jones matrix $J_{x,y,z}$. If the light travels parallel to the z-axis, for each row of cells x, y we compute the effect that the row has on the light.

$$J_{x,y} = J_A \left(\prod_{i=0}^{L/ds} J_{x,y,z+i\,ds} \right) J_P \qquad (1.19)$$

The next step is to compute the intensity $I_{x,y}$ of the light for each row of cells x, y. By setting the ingoing light intensity to 1, after the first polarizer P, $I_{x,y}$ gives the transmission intensity of the pixel located at x, y, after the analyzer.

In Figure 1.3 and Figure 1.4 we report two examples, where the direction of the polarizer (P) and the analyser (A) are shown by arrows. The colorscale is set so that white means maximal intensity and black zero intensity, with a blue scale in between.
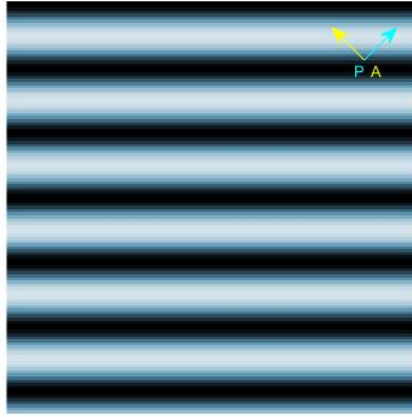
Figure 1.3: Simulation of the bulk cholesteric nematic field, equation (1.1)
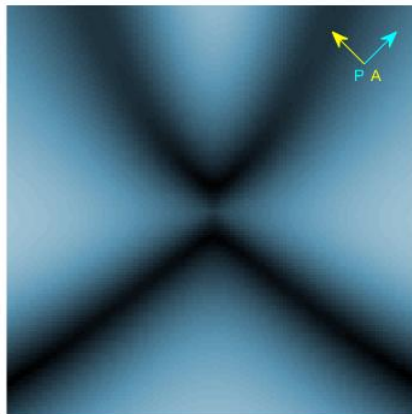
Figure 1.4: Simulation of another nematic field

2. The Experimental System

In this chapter we introduce and describe the experimental system and we are going to study the results reported come from [2] and [15].

2.1 The system

In [2] and [15] the authors analysed the liquid-crystalline behaviour of amyloid fibrils generated from β-lactoglobulin, dispersed in water solution. The amyloid fibrils considered in [2] and [15] are rod-like particles of width 4 nm and length 400 nm, much bigger than the classical PAA and MBBA liquid crystals, introduced in Chapter 1.

It has been shown that, there is a concentration at which the cholesteric bulk phase separates from the isotropic bulk phase [2]. When a solution of water and amyloid fibrils is brought to a certain critical concentration, birefringent domains start to nucleate and grow, eventually leading to a bulk anisotropic phase. These domains of nematic or cholesteric solution are surrounded by isotropic fluid. They are often called *tactoids* and were observed for nematic liquid crystal already in [16] and [17]. In the present context, the most important effect that was shown is the formation of four different droplet shapes, which were characterized by cross-polarized microscopy.

At increasing droplet volume, the first phase that appears is the so called *homogeneous* tactoid. In Figure 2.1 we see an example of it, the uniform
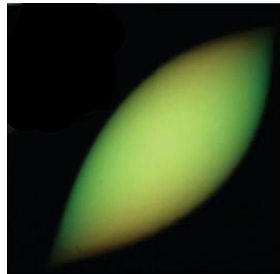
Figure 2.1: Homogeneous tactoid seen through a cross-polarized microscopy.

colour representing an homogeneous nematic field. The name derives from the constant nematic field measured on the inside. From this droplet, we can

measure the aspect ratio, defined as the ratio between the major and the minor axis, and the tip angle.
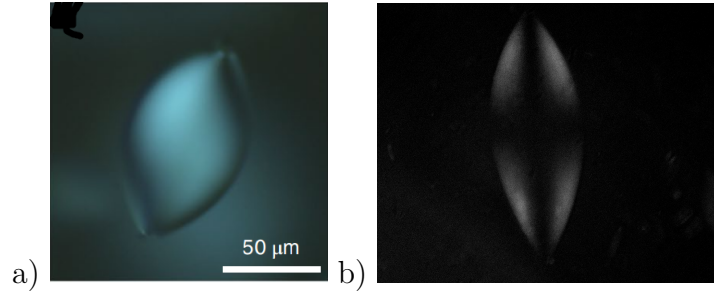
Figure 2.2: Cross-polarized microscopy images of the bipolar droplet in case of polarizers at 45° from the major axis (a), and aligned with the axis (b).

The second droplet is called *bipolar* tactoid. Similarly to the homogeneous case, we can measure the aspect ratio and the tip angle. Nevertheless, a bipolar droplet shows a characteristic dark cross when the polarizers are aligned with the axes of the tactoid (Figure 2.2). In this case, the nematic field is directed from one pole to the other. The homogeneous and bipolar droplets are typical of nematic liquid crystals. Their shape is symmetrical around their major axis and its often referred to as *spindle-like*. A theoretical analysis of these droplets and the transition between the two can be found in [3] and [18].

The third shape that appears is called *uniaxial cholesteric* droplet, shown in Figure 2.3(a). From this droplet we are able to measure the aspect ratio and the
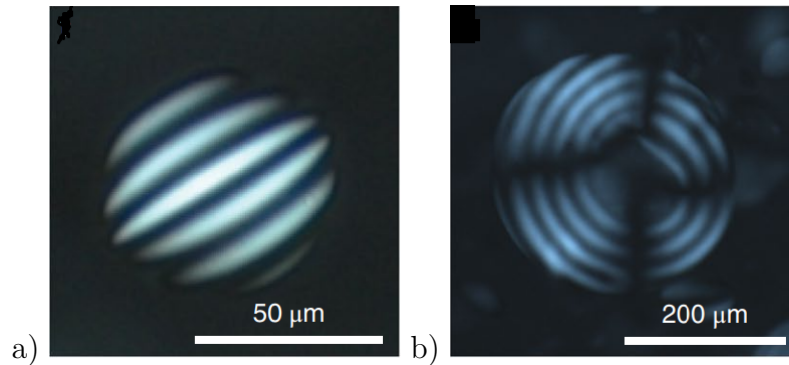
Figure 2.3: Cross-polarized microscopy images of the cholesteric droplet (a), and of the onion droplet (b).

pitch of the cholesteric phase, that is twice the distance between consecutive light bands. In [2] the authors analysed the shape of these droplets and found out that they are prolate ellipsoids with the birefringent bands parallel to the major axis, i.e. the cholesteric axis runs parallel to a minor axis.

The last shape is called *onion*, shown in Figure 2.3(b). As for the cholesteric, we can measure the pitch and the aspect ratio of these droplets. The onion tactoids have also been observed in [19].

2.2 Experimental data

In Figure 2.4, we report the aspect ratio and the family of the tactoids as a function of their volume, as obtained by the experiments performed in [15].
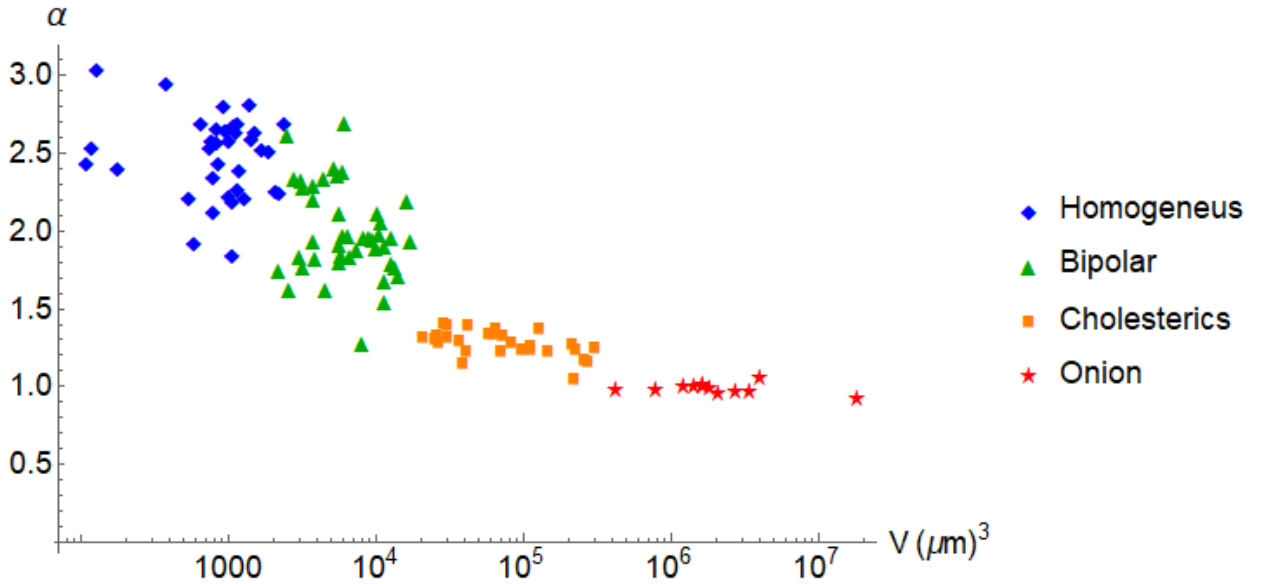
Figure 2.4: Plot of the Aspect ratio α as a function of the volume V.

It can be observed that, with increasing volume, the various shapes appear and the aspect ratio of the droplets decreases.

Figure 2.5 shows the relationship between the tip angle Θ and the aspect ratio for bipolar droplets. In the figure can be seen that as the aspect ratio
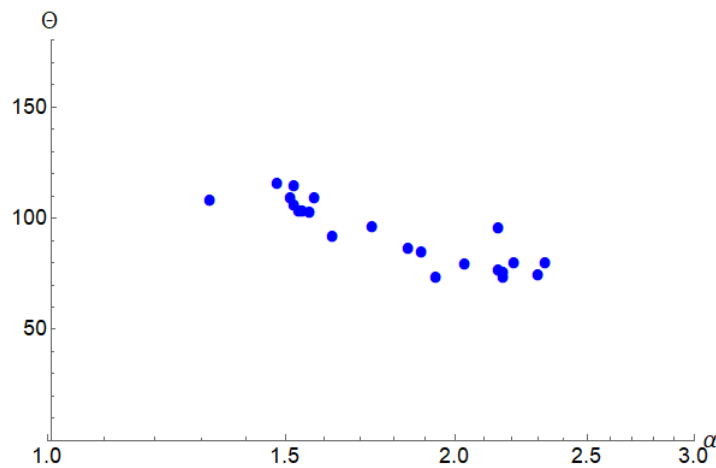
Figure 2.5: Plot of the tip angle Θ (in degrees) as a function of the aspect ratio α, for bipolar droplets .

decreases the tip angle increases, therefore the bipolar droplets tend to become more spherical, i.e. $\alpha = 1$ and $\Theta = 180°$, as the volume decreases.

Figure 2.6 shows the pitch, measured as twice the band-to-band distance, as a function of volume for cholesterics and onions.
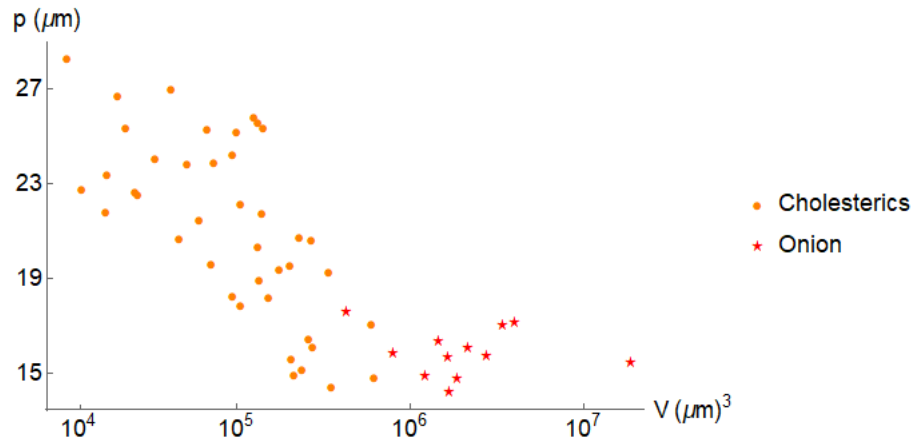
Figure 2.6: Plot of the pitch p as a function of the volume V.

From the graph, it is clear that in cholesteric tactoids the pitch decreases with the droplet volume. In contrast, the periodicity is stable for the onion droplets and has value equal to the natural pitch of $p_\infty = 15\mu m$, measured in the bulk cholesteric phase. For further details of the measurements see [15].

A complete theoretical model of the system is still missing. In the following work, our aim is to present some physical models that are able to describe the features displayed by these droplets.

The theoretical framework used will be presented in the following chapters. We will tackle the issue by a variational approach, i.e. by postulating a reasonable analytic formula for the nematic field of the case at hand and minimizing the free energy by suitably tuning the parameters of the model. As building blocks we will employ the Frank-Oseen free energy [20], paired with an anisotropic surface tension [21].

3.   The Bulk energy

In this chapter we introduce the classical theory of liquid crystals, based on the works of Oseen [22], Zocher [23] and Frank [20].

3.1   Preliminaries

We assume that the region occupied by the liquid crystal is a regular 3-dimensional region $\mathcal{B}$.

We will call $\partial \mathcal{B}$ the boundary of $\mathcal{B}$, and assume it has a finite surface area, where ν will be the unit normal to the surface.

The orientation of the director field is given by the map:

$$n : \mathcal{B} \to \mathbb{S}^2 \tag{3.1}$$

where $\mathbb{S}^2 = \left\{ v \in \mathbb{R}^3 : v \cdot v = 1 \right\}$.

The functional for the bulk free energy F_B is assumed to depend only on n and its first derivatives

$$F_B(n) = \int_{\mathcal{B}} f(n, \nabla n) dV, \tag{3.2}$$

where $f : \mathcal{B} \to \mathbb{R}$ is the free-energy density. f must obey some physical requirements, arising from the symmetry properties of the liquid crystal, namely:

- Frame invariance

- Evenness

- Material symmetry

- Positive definiteness

3.1.1   Frame invariance

The energy density, being a scalar physical quantity, must be the same in two different frames, rigid or deformable.

Let $p \in \mathcal{B}$, we identify a frame with origin on p with (e_1, e_2, e_3) and a second one with (e_1', e_2', e_3'). Let Q be a linear map from $\mathbb{R}^3 \to \mathbb{R}^3$. Since the vector n is in the submanifold $\mathbb{S}^2 \subset \mathbb{R}^3$, the only linear maps $Q : \mathbb{S}^2 \to \mathbb{S}^2$ are given by

$$Q \in \mathrm{O}(3) = \left\{ Q : Q^T Q = \mathbb{I} \right\}, \tag{3.3}$$

or the subset

$$\mathrm{SO}(3) = \left\{ Q : Q^T Q = \mathbb{I} \wedge \det(Q) = 1 \right\} \subset O(3). \tag{3.4}$$

We limit the discussion to $\mathrm{SO}(3)$, the case of $O(3)$ will be dealt with in the next paragraph. Let $Q \in \mathrm{SO}(3)$ such that :

$$e_i = Q e_i' \tag{3.5}$$

The components of n in the two frames are

$$n_i = n \cdot e_i \qquad n_i' = n \cdot e_i'. \tag{3.6}$$

Through (3.5), we can relate n_i' to n_i

$$n_i' = n \cdot e_i' = n \cdot Q^T e_i = Q n \cdot e_i = Q_{ij} n_j, \tag{3.7}$$

and arrive to

$$n' = Qn. \tag{3.8}$$

From differential geometry we know that

$$\nabla' = Q\nabla, \tag{3.9}$$

where ∇ and ∇' are the derivative operators in the reference frames identified by e and e', respectively. It is easy to show that

$$\nabla' n' = Q\nabla(Qn) = Q\nabla n Q^T \tag{3.10}$$

The assumption of frame invariance implies for the free energy density that

$$f(Qn, Q\nabla n Q^T) = f(n, \nabla n) \tag{3.11}$$

for every $p \in \mathcal{B}$, $n \in \mathbb{S}^2$ and $Q \in \mathrm{SO}(3)$.

3.1.2 Evenness

Generally, it is assumed that for both nematics and cholesterics one cannot distinguish the head from the tail. Thus, n and $-n$ must be indistinguishable, implying that the energy density must not be affected by a change of sign of n:

$$f(n, \nabla n) = f(-n, -\nabla n) \tag{3.12}$$

3.1.3 Material Symmetry

In the previous paragraph, we restricted the class of maps $Q : \mathbb{S}^2 \to \mathbb{S}^2$ to SO(3), however the most general case is given by O(3). The difference lies in reflections. Condition (3.11) applies to both nematic and cholesterics, however under reflections nematic and cholesterics behave differently: these are called *material symmetries* [24]. While nematic liquid crystals remain alike after a reflection, cholesterics suffer a change in chirality. This means that a reflection may change the energy density of cholesteric liquid crystals.

To be more precise, let $p \in \mathcal{B}$ and $v \in \mathbb{S}^2$. We can write the reflection across the plane orthogonal to v [25] as

$$R(v) = \mathbb{I} - 2vv^T \tag{3.13}$$

where $\mathbb{I}$ is the identity and vv^T the matrix whose ij element is $v_i v_j$. The tensor $R(v)$ is obviously symmetric and such that $R(v)^2 = \mathbb{I}$, i.e. R belongs to O(3). The determinant of R is -1, since the eigenvalues are $1, 1$ and -1. Therefore, it doesn't belong to SO(3). However $-R$ belongs to SO(3), since $\det(-R) = (-1)^3 \det(R) = 1$. Now, let us apply R to the nematic field:

$$n' = Rn \qquad \nabla'n' = R\nabla n R \tag{3.14}$$

For a nematic field, f must be invariant under this transformation, thus

$$f(n', \nabla'n') = f(n, \nabla n) \tag{3.15}$$

which reduces to

$$f(Rn, R\nabla n R) = f(n, \nabla n) \tag{3.16}$$

We can write equation (3.16) such that

$$f((-R)(-n), (-R)\nabla n(-R)) = f(-n, \nabla n) \tag{3.17}$$

by equation (3.11) and $-R \in$ SO(3). In contrast, for cholesterics $f(-n, \nabla n) \neq f(n, \nabla n)$. Therefore the material symmetries can be summarized as follows

$$f(Qn, Q\nabla n Q^T) = f(n, \nabla n) \tag{3.18}$$

where

$$Q \in \begin{cases} \text{O(3)} & \text{for nematics,} \\ \text{SO(3)} & \text{for cholesterics.} \end{cases} \tag{3.19}$$

3.1.4 Positive definiteness

The free energy of a system is defined within an addictive constant. On the other hand, when no external forces or boundary conditions (e.g. anchoring)

affect the liquid crystal, it relaxes to the natural state. We define this natural orientation n as the nematic field such that $f(n, \nabla n) = 0$.

Therefore we require f to reach its minimum in case of a natural orientation. This means that for a general vector field n

$$f(n, \nabla n) \geq 0. \tag{3.20}$$

3.2   Frank's formula

In this section, following [24], we want to determine the formula for the bulk energy of nematic and cholesteric liquid crystals, mainly developed by Frank in [20].

The simplest scalar function depending on a vector n and quadratically on a tensor N [24], is the following

$$f(n, N) = f_0(n) + f_1(n) \cdot N + N \cdot f_2(n)N \tag{3.21}$$

where f_0 is a scalar function of n, f_1 is a tensor depending on n, and f_2 is a symmetric second order tensor depending on n.

We are interested in the case where $N = \nabla n$. We will assume that distortions are large compared to the typical length scale, given by the molecular length a

$$\|\nabla n\| \ll a^{-1} \tag{3.22}$$

therefore we can neglect higher orders terms in N.

Equation (3.21) can be rewritten as follows:

Theorem 3.1. *Let n be a unitary vector field defined as above, and f of the form* (3.21) *obeying the physical requirements of* frame invariance, evenness, material symmetry and positive definiteness f *can be rewritten as*

$$
\begin{aligned}
f_B(n, \nabla n) = & K_1(\nabla \cdot n)^2 + K_2(n \cdot \nabla \times n - q_\infty)^2 + \\
& + K_3(n \times \nabla \times n)^2 + K_{24}\left(\mathrm{tr}\left((\nabla n)^2\right) - (\nabla \cdot n)^2\right)
\end{aligned} \tag{3.23}
$$

where K_i ($i = 1, 2, 3, 24$) and q_∞ are scalars. K_1, K_2 and K_3 are called splay, twist *and* bend *moduli,respectively, while K_{24} will be called* saddle-splay *modulus, and finally q_∞ is called* natural twist.

Before proving the theorem above, we introduce some useful vector identities.

Lemma 3.2. *Each antisymmetric matrix A, i.e. satisfying $A = -A^T$, can be written in the form*

$$A_{ij} = a_k \varepsilon_{ijk} \tag{3.24}$$

where a is called axial vector *of A.*

For the proof see [25].

Let ∇v be the derivative of a vector field v, then the axial vector of the antisymmetric part of ∇v is called the *curl* of v, and it is written as

$$\nabla \times v \tag{3.25}$$

Lemma 3.3. *Let n be unity a vector field. On the domain of n the following identities hold:*

1. $(\nabla n)^T n = 0$;

2. $(\nabla n)n = (\nabla \times n) \times n$;

3. $(\nabla \times n)^2 = (n \cdot \nabla \times n)^2 + (\nabla \times n \times n)^2$;

4. $\nabla n \cdot \nabla n = \text{tr}\left((\nabla n)^2\right) + (\nabla \times n)^2$.

Proof. (1) Since n is a unitary vector field $n \cdot n = 1$. Applying ∇ we get

$$(\nabla n)^T n = \frac{1}{2}\nabla(n \cdot n) = \nabla(1) = 0. \tag{3.26}$$

(2) Adding and subtracting $(\nabla n)^T$ we get

$$(\nabla n) = \frac{1}{2}\left((\nabla n) + (\nabla n)^T\right) + \frac{1}{2}\left((\nabla n) - (\nabla n)^T\right) =: S + W \tag{3.27}$$

Where S is symmetric and W antisymmetric. Applying both S and W to n and using identity *1* we get

$$Sn = Wn, \tag{3.28}$$

therefore

$$(\nabla n)n = Sn + Wn = 2Wn. \tag{3.29}$$

Since the axial vector of W is by definition $\nabla \times n$, this means that

$$(\nabla n)n = \nabla \times n \times n \tag{3.30}$$

(3) Let a and $b \in \mathbb{R}^3$, then

$$\|a\|^2\|b\|^2 = (a \cdot b)^2 + \|a \times b\|^2. \tag{3.31}$$

From $\|a \times b\|^2 = \|a\|^2\|b\|^2 - (a \cdot b)^2$, substituing $a = \nabla \times n$ and $b = n$ we get

$$\|\nabla \times n\|^2\|n\|^2 = (\nabla \times n \cdot n)^2 + \|\nabla \times n \times n\|^2. \tag{3.32}$$

The identity follows from $\|n\| = 1$.

(4) To prove the fourth identity, first we take the trace of the square of (3.27)

$$\text{tr}\left((\nabla n)^2\right) = \text{tr}S^2 + \text{tr}(SW + WS) + \text{tr}W^2; \tag{3.33}$$

since $WS + SW$ is antisymmetric[1], it is traceless and the previous reduces to

$$\text{tr}\left((\nabla n)^2\right) = \text{tr}(S^2) + \text{tr}(W^2). \tag{3.34}$$

Taking the scalar product of (3.27) with itself, gives

$$(\nabla n)(\nabla n) = S \cdot S + 2S \cdot W + W \cdot W, \tag{3.35}$$

The three addenda are respectively $S \cdot S = S \cdot S^T = \text{tr}(S^2)$, $S \cdot W = 0$, and $W \cdot W = -W \cdot W^T = -\text{tr}(W^2)$. It is easy to see that

$$2W \cdot W = (\nabla \times n)^2. \tag{3.36}$$

Substituting (3.33) into (3.35), and using (3.36) we arrive at

$$(\nabla n)(\nabla n) = \text{tr}\left((\nabla n)^2\right) + (\nabla \times n)^2. \tag{3.37}$$

$\square$

The frame invariance gives this result
Lemma 3.4. *The function* (3.21) *obeys*

$$f(Qn, QNQ^T) = f(n, N), \tag{3.38}$$

for every $Q \in \text{O}(3)$, *if and only if,*

$$\begin{aligned}
f(n, N) = {} & \alpha_0 + \alpha_1 P(n) \cdot N + \alpha_2 W(n) \cdot N + \\
& + \beta_1 (W(n) \cdot N)^2 + \beta_2 (P(n) \cdot N)^2 + \beta_3 (P(n) \cdot N)(W(n) \cdot N) + \\
& + \beta_4 N \cdot N + \beta_5 P(n) N \cdot (N) P(n)
\end{aligned} \tag{3.39}$$

where α_i *(i = 0, 1, 2) and* β_i *(i = 1, . . . , 5) are scalars. While*

$$P(n)_{ij} = \delta_{ij} - n_i n_j \tag{3.40}$$
$$M(n)_{ik} = \varepsilon_{ijk} n_j \tag{3.41}$$

Proof. The proof can be found in [24], it is strictly technical and involves using the properties of O(3). $\square$

To prove theorem 3.1 we evaluate (3.39) for $N = \nabla n$.

Proof of theorem 3.1. Recalling the definition of $P(n)$, taking the scalar product with ∇n and using identity *1.* we get

$$P(n) \cdot (\nabla n) = \text{tr}(\nabla n) + n \cdot (\nabla n)^T n = \text{tr}(\nabla n) = \nabla \cdot n, \tag{3.42}$$

where $\text{tr}(\nabla n)$ is by definition the divergence of n.

---

[1]Taking the transpose proves the statement.

Taking the scalar product of $M(n)$ with (∇n), we have

$$M(n) \cdot (\nabla n) = M(n) \cdot W = n \cdot \nabla n, \tag{3.43}$$

since $M(n)$ is the antisymmetric tensor with n as axial vector.

The last piece missing is given by

$$P(n)\nabla n \cdot \nabla n P(n) = \nabla n \cdot \nabla n - (\nabla n n)^2 = \mathrm{tr}\nabla n^2 + (n \cdot \nabla n)^2, \tag{3.44}$$

from identities $2, 3$ and 4. Substituting into (3.21) and setting

$$\beta_1 =: K_{24} - K_2, \qquad\qquad \beta_2 =: K_1 - K_{24}, \tag{3.45}$$
$$\beta_4 =: K_3, \qquad\qquad \beta_5 =: K_{24} - K_3. \tag{3.46}$$

$f(n, \nabla n)$ takes the form

$$\begin{aligned}
f(n, \nabla n) = {} & \alpha_0 + (\alpha_2 + \beta_3 n \cdot \nabla \times n)(\nabla \cdot n) + \alpha_3(n \cdot \nabla \times n) + \\
& K_1(\nabla \cdot n)^2 + K_2(n \cdot \nabla \times n)^2 + K_3(n \times \nabla \times n)^2 + \\
& K_{24}\left(\mathrm{tr}\nabla n^2 - (\nabla \cdot n)^2\right)
\end{aligned} \tag{3.47}$$

From the evenness property we know that

$$f(-n, -\nabla n) = f(n, \nabla n) \tag{3.48}$$

therefore $\alpha_2 = 0 = \beta_3$.

In the case of nematics,

$$f(-n, \nabla n) = f(n, \nabla n) \tag{3.49}$$

holds true, therefore $\alpha_3 = 0$, and from the positive definiteness $\alpha_0 = 0$, since the natural orientation is a constant field ($\nabla n = 0$).

For cholesterics instead, the natural orientation is given by (1.1). The only non-zero term is $(n_c \cdot \nabla \times n_c) = q_\infty$. From the positive definiteness we get

$$f(n_c, \nabla n_c) = \alpha_0 + \alpha_3 q_\infty + K_2 q_\infty^2 = 0, \tag{3.50}$$

therefore

$$-\alpha_3 = \frac{\alpha_0}{q_\infty} + K_2 q_\infty \tag{3.51}$$

setting $\alpha_0 = K_2 q_\infty^2$, f takes the same form for both nematics and cholesterics, where nematics are a special case of cholesterics with $q_\infty = 0$. $\qquad\square$

3.2.1 Second-order energies

In 1971 Nehring and Saupe [26] allowed the free energy density to depend up to the second derivatives of n. By imposing the same requirements to get to the Frank's energy, only one additional term comes out, equipped with the elastic modulus K_{13}:

$$f_{13} := K_{13}\nabla \cdot ((\nabla \cdot n)n), \tag{3.52}$$

K_{13} is sometimes called *splay-bend* elastic modulus.

3.2.2   Null Lagrangians

The reader may wonder why the divergence terms in (3.23) are not summed together. The reason is that

$$\mathrm{tr}(\nabla n)^2 - (\nabla \cdot n)^2 \qquad (3.53)$$

is a *null lagrangian*. A null lagrangian is an energy density term that can be expressed as a divergence, and via Gauss' Theorem, it can be transformed into a surface energy density.

Let

$$m := (\nabla n)n - (\nabla \cdot n)n, \qquad (3.54)$$

By taking the divergence of m we get

$$\nabla \cdot m = \mathrm{tr}(\nabla n)^2 - (\nabla \cdot n)^2 + n^j \left(\nabla_i \nabla_j n^i - \nabla_j \nabla_i n^i \right) \qquad (3.55)$$

that is clearly our saddle-splay energy since the derivatives commute. Therefore via Gauss theorem,

$$\int_{\mathcal{B}} \nabla \cdot m \, dV = \int_{\partial \mathcal{B}} m \cdot \nu dS \qquad (3.56)$$

Both K_{24} and K_{13} can be expressed as integrals over the surface of $\mathcal{B}$. They do not enter the bulk free energy, however they contribute to equilibrium solutions through the boundary conditions at the surface.

3.2.3   The theoretician's energy

Assuming $K_1 = K_2 = K_3 = K_{24} = K$ and $K_{13} = 0$, and $q_\infty = 0$ we get the so called *one-constant approximation*, or *theoretician's energy*, and (3.23) takes the form

$$f_F(n, \nabla n) = K(\nabla n) \cdot (\nabla n). \qquad (3.57)$$

Equation (3.37) and identity 3. from lemma 3.3 are enough to prove the statement.

3.3   Frank's constants

Since the derivatives of n have a dimension of the inverse of a length, the coefficients K_i have the dimension of an energy over a length, that is a force. A typical energy value for liquid crystal is given by $k_B T_c \approx 4 \cdot 10^{-21}$ where T_c is the clearing temperature, while the typical distance is given by the molecular scale $a \approx 10^{-9}$m, therefore a typical value of K is

$$K \sim \frac{k_B T_c}{a} \approx 10^{-11} N \qquad (3.58)$$

For thermotropic liquid crystals the constants depend on the temperature T. The first experimental data came from Zvetkov in 1937 [27], which measured for MBBA at $T = 125^oC$

$$K_1 = 2.3 \cdot 10^{-11} N \qquad K_2 = 1.5 \cdot 10^{-11} N \qquad K_3 = 4.8 \cdot 10^{-11} N \qquad (3.59)$$

In most cases the twist constant K_2 is the smallest one. In De Gennes [4] the values of the elastic constants can be found for PAA and MBBA at various temperatures. Very little is known about K_{24} since until very recently no experiment was arranged to measure it, see [28], while nothing is known about K_{13}.

We want to interpret each elastic modulus. Following [20] we produce four different director fields and calculate the free energy density f. The elastic constants appear independently of each other, except for K_{24}.

3.3.1   Splay modulus

Let $\mathcal{B}$ be parametrized by cylindrical coordinates (r, θ, ϕ). Let $n_s = e_r$ (Figure 3.1(a)) be the nematic field. Therefore the derivative of the field is

$$\nabla \cdot n_s = \frac{1}{r} \qquad \nabla \times n_s = 0 \qquad (3.60)$$

Therefore, for a nematic liquid crystal ($q_\infty = 0$), the energy density is

$$f(n_s, \nabla n_s) = K_1 \frac{1}{r^2}. \qquad (3.61)$$

Except for the line where $r = 0$, the energy density for this field depends only on K_1.

This is a case of a line defect, where the energy diverges in any neighbourhood containing the z-axis. In cylindrical coordinates, it is sufficient to integrate around a cylinder aligned with the z-axis.

$$F_B(n_s) = K_1 \int \frac{1}{r^2} r \, dr d\theta dz = K_1 \int \frac{1}{r} \, dr d\theta dz \qquad (3.62)$$

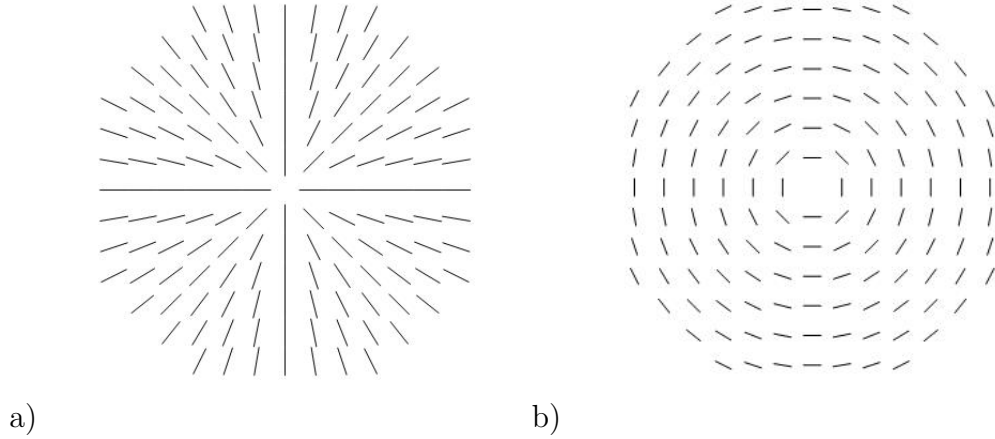in this case the integral clearly diverges for $r \to 0$.

3.3.2   Bend modulus

Keeping the same coordinate system of the example before, we define the nematic field (Figure 3.1(b))

$$n_b := e_\theta \qquad (3.63)$$

In this case the divergence is null, while the curl

$$\nabla \times n_b = \frac{1}{r^2} e_z \qquad (3.64)$$

a)   b)

Figure 3.1: (a) Vector plot of n_s, at $z = 0$;(b) Vector plot of n_b, at $z = 0$.

Therefore, the energy density is

$$f(n_b, \nabla n_b) = K_3 \frac{1}{r^2}. \tag{3.65}$$

As before, around the z-axis the energy density of n_b depends only on K_3.

These two fields, n_s and n_b both display infinite energy defects in a cylinder around z. If $K_1 = K_3$ then they have the same energy density.

3.3.3   Twist modulus

Let $\mathcal{B}$ be parametrized with Cartesian coordinates (x_1, x_2, x_3), and have the following nematic field, dependent on q and ϕ:

$$n_t = \cos(qx_3 + \varphi)e_1 + \sin(qx_3 + \varphi)e_2 \tag{3.66}$$

The energy density becomes for nematics
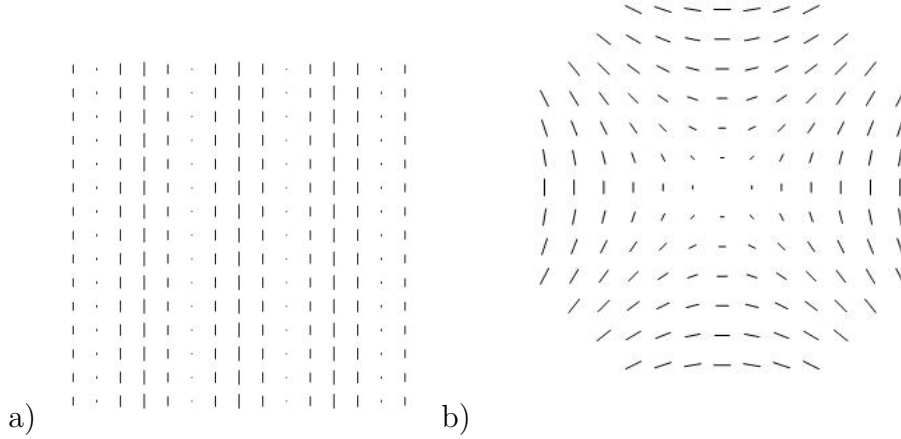
$$f(n, \nabla n) = K_2 q^2. \tag{3.67}$$

The free energy depends only on K_2, and increases quadratically with q, which is often referred as *twist*.

In case of cholesterics the twist density becomes

$$f(n, \nabla n) = K_2(q - q_\infty)^2 \tag{3.68}$$

whose minimum is at $q = q_\infty$. This represents a natural equilibrium state for a cholesteric in absence of boundary conditions.

Figure 3.2: (a) Vector plot of n_t, at $z = 0$;(b) Vector plot of n_ϕ, at $z = 0$.

3.3.4   Saddle-splay Modulus

To provide an interpretation of the Saddle-splay modulus, suppose that $\mathcal{B}$ is parametrized by Cartesian coordinates (x, y, z). Then we take the function

$$\phi(x, y, z) := z - xy \tag{3.69}$$

and use its unit gradient as nematic vector field (Figure 3.2(b)),

$$n_\phi := \frac{\nabla \phi}{\|\nabla \phi\|} = \frac{(-y, -x, 1)}{\sqrt{1 + x^2 + y^2}}. \tag{3.70}$$

We calculate the energy terms

$$\nabla \cdot n = \frac{2xy}{(1 + x^2 + y^2)^{3/2}} \tag{3.71}$$

$$\nabla \times n = \frac{(y^2 - x^2, -x, y)}{(1 + x^2 + y^2)^{3/2}} \tag{3.72}$$

$$\mathrm{tr}(\nabla n)^2 = \frac{2x^2 y^2}{(x^2 + y^2 + 1)^3} + \frac{2 \left(x^2 + 1\right) \left(y^2 + 1\right)}{(x^2 + y^2 + 1)^3} \tag{3.73}$$

In a ε-neighbourhood of the origin the energy density can be expressed as

$$f_\phi = 2K_{24} + O(\varepsilon) \tag{3.74}$$

Therefore in a neighbourhood of the origin n_ϕ is a saddle-splay field.

4. Drops

In this chapter, we discuss the free-boundary problems for liquid crystals. We introduce the anisotropic surface tension and discuss the equilibrium shapes of a drop surrounded by isotropic fluid, which leads to the Wulff's construction, presented in the last paragraph.

4.1 Surface free energy

Liquid crystals are incompressible fluids, therefore even though the shape may not be prescribed, its volume is fixed

$$\int_{\mathcal{B}} dV = V \tag{4.1}$$

In our analysis, the droplet is surrounded by isotropic fluid, and it is well known that the free energy associated with the surface, called *isotropic surface tension*, is proportional to the area and to a positive constant γ depending on the nature and temperature of the fluids in contact.

However, the isotropic surface tension is not enough to describe the whole surface energy. Liquid crystals are anisotropic, therefore as suggested by Oseen [29] it should have a more general formulation depending on the direction of the nematic field n and the normal to the surface, ν. The more general functional that can be written is

$$F_S(\mathcal{B}, n) = \gamma \int_{\partial \mathcal{B}} f_S(n, v) da \tag{4.2}$$

often called *anisotropic surface tension*. Since f_S has to be frame invariant, and both n and v are unit vectors, f_S can only take the form (see [30] for a rigorous proof)

$$f_S(n, v) = f_S(|n \cdot v|). \tag{4.3}$$

The dot product is the cosine of the angle between them, therefore

$$f_S(n, v) = f_S(\cos \theta). \tag{4.4}$$

The next question to answer is the form of f_S, we set

$$f_S(\cos \theta) = 1 + \omega \cos^2 \theta. \tag{4.5}$$

where $\omega > -1$. This formula was introduced by Rapini and Papoular [21] and has been confirmed by several experiments, for example see [31].

For $\omega = 0$ we get the isotropic surface tension, for $-1 < \omega < 0$ we get a favoured homeotropic alignment, while for $\omega > 0$ we get a favoured tangential alignment.

The bulk term of the free energy of a drop is given by the Frank-Oseen energy

$$F_B(\mathcal{B}, n) = \int_{\mathcal{B}} f_B(n, \nabla n) dV \tag{4.6}$$

Then we can write the total energy of a drop of nematic liquid crystals surrounded by an isotropic fluid as

$$F(\mathcal{B}, n) = F_B(\mathcal{B}, n) + F_S(\mathcal{B}, n) \tag{4.7}$$

where the anistropic tension is given by (4.5). A configuration of the drop, that is the couple $(\mathcal{B}, n)$, is said to be a stable equilibrium configuration if F is minimized by the configuration.

Let us define a change of variables in $\mathcal{B}$, such that

$$y = \frac{x}{V^{1/3}} \tag{4.8}$$

where V is the volume of $\mathcal{B}$. The volume of $\mathcal{B}' = y(\mathcal{B})$ is 1. On $\mathcal{B}'$ we define:

$$n'(y) = n(xV^{1/3}) \qquad \nabla n'(y) = V^{1/3}\nabla n(V^{1/3}x) \tag{4.9}$$

Therefore is it easy to see that F can be written in the form

$$F = V^{1/3}F_B(\mathcal{B}', n') + V^{2/3}F_S(\mathcal{B}', n') \tag{4.10}$$

In the limit where V tends to 0, the drop is small and the bulk energy term prevails.

Therefore, for $V \to 0$, F can be approximated as

$$F = V^{1/3}F_B(\mathcal{B}', n') \tag{4.11}$$

In case of nematics, F is minimized by the natural configuration given by a constant field $n = n_e$.

What does it mean that the drop is small in physical terms? Let ℓ be the ratio

$$\ell := \frac{F_B(\mathcal{B}', n')}{F_S(\mathcal{B}', n')}. \tag{4.12}$$

A rough estimate of ℓ can be given by the single constant approximation where

$$\ell := \frac{K}{\gamma}. \tag{4.13}$$

For volumes smaller than ℓ^3, the approximation of equation (4.11) holds.

For example, data from Langevin [32] (MBBA at $T = 25°C$) give $\ell \sim 10^{-10}$m, therefore any possible drop has to be considered large, independently of their actual size. While in [2], the ratio K/γ has been measured to be $\ell \sim 5\,\mu$m, therefore any droplet of volume $V < (5\,\mu\text{m})^3$ can be considered small.

When $V^{1/3} < \ell$ the equilibrium shape of the droplet is obtained by minimizing F_S with $n = n_e$.

$$F_S = \gamma \int_{\partial\mathcal{B}} f_S(\nu \cdot n_e) dS \tag{4.14}$$

with the constraint $\int_{\mathcal{B}} dV = V$.

This problem was solved with a construction first considered by Wulff in 1901, which will be examined in the following section.

4.2 Wulff's construction

In 1901 Wulff [33], studying the growth of crystals, developed the following model. Let us consider the functional given by:

$$F[\mathcal{B}] := \gamma \int_{\partial\mathcal{B}} \left(1 + \omega(\nu \cdot n)^2\right) da \tag{4.15}$$

where $\mathcal{B}$ is such that $\int_{\mathcal{B}} dV = V$, ν is the unit normal to the surface and n is a constant vector. The set $\mathcal{B}$ minimizing (4.15) results from the so called *Wulff's construction*. Wulff conjectured that is unique; a more general and in-depth discussion can be found in [34].

In the following, it will be assumed that the liquid crystal is nematic ($q_\infty = 0$). We will use cylindrical coordinates (ρ, θ, z) with the z-axis fixed along n, $n = e_z$. In addition, we will suppose that $\mathcal{B}$ has a cylindrical symmetry around e_z, so the surface can be parametrized by the curve $\rho(z)$. The symmetry for reflections in the plane $z = 0$ implies $\frac{d\rho}{dz}(0) = 0$. To simplify the notation we define $\upsilon := \frac{d\rho}{dz}$, thus the infinitesimal area becomes $da = \sqrt{1 + \upsilon^2}dz$, and the scalar product $(\nu \cdot n) = -\upsilon/\sqrt{1 + \upsilon^2}$.

As boundary conditions we impose $\rho(0) = r$ and $\rho(\pm R) = 0$, where r and R are constrained so that the volume of the region is V.

Equation (4.15) becomes

$$F(\rho, \upsilon) = 2\pi\gamma \int_{-R}^{R} \left(\rho\left(1 + \omega\frac{\upsilon^2}{1 + \upsilon^2}\right)\sqrt{1 + \upsilon^2}\right) dz, \tag{4.16}$$

where the constants outside the integral can be dropped, since we are interested in the minimum.
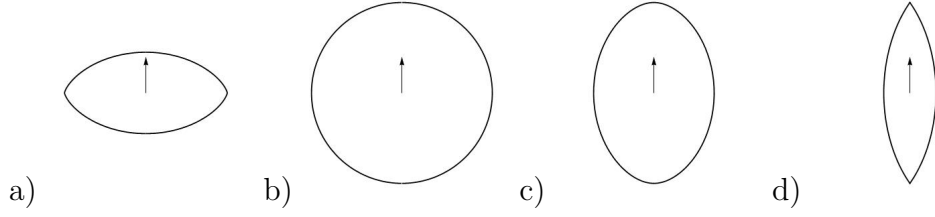
Figure 4.1: Various shapes of the Wulff drop for $\omega = -0.5, 0, 0.5, 3$ respectively, the arrow represents the direction of the director field.

Using the Lagrangian multipliers we can impose the constraint on the volume

$$\tilde{F}(\rho, \upsilon) = \int_{-R}^{R} \left(\rho \left(1 + \omega \frac{\upsilon^2}{1 + \upsilon^2} \right) \sqrt{1 + \upsilon^2} - \lambda \left(\frac{1}{2} \rho^2 - \frac{V}{2R} \right) \right) dz \qquad (4.17)$$

Instead of solving the Euler-Lagrange equations, we apply the Beltrami identity, which ensures that the quantity $L - \upsilon \frac{\partial L}{\partial \upsilon}$ is a constant, where L is the integrand of equation (4.17). We get

$$\left(\frac{\lambda V}{2R} + \frac{\rho \left(1 - \upsilon^2 (\omega - 1) \right)}{(\upsilon^2 + 1)^{3/2}} - \frac{\lambda \rho^2}{2} \right) = C, \qquad (4.18)$$

Since $\rho(\pm R) = 0$, $C = V \frac{\lambda}{2R}$ and we get the following function as a first integral

$$H(\rho, \upsilon) = \rho \left(\frac{1 - \upsilon^2 (\omega - 1)}{(\upsilon^2 + 1)^{3/2}} - \frac{\lambda \rho}{2} \right) \qquad (4.19)$$

in our case, since $\rho(\pm R) = 0$, the orbit on the phase space (ρ, υ) lies on the implicit curve $H(\rho, \upsilon) = 0$. This gives

$$\rho(\upsilon) = \frac{2}{\lambda} \cdot \frac{1 - \upsilon^2 (\omega - 1)}{(\upsilon^2 + 1)^{3/2}} \qquad (4.20)$$

We know that $\rho(z = 0) = r$ and $\upsilon(z = 0) = 0$, thus we have $\rho(\upsilon = 0) = r$:

$$\rho(\upsilon = 0) = \frac{2}{\lambda} = r. \qquad (4.21)$$

This gives

$$\rho(\upsilon) = r \frac{1 - \upsilon^2 (\omega - 1)}{(\upsilon^2 + 1)^{3/2}}. \qquad (4.22)$$

Solving for $\rho = 0$ we get the value of υ at $z = \pm R$, that is

$$\upsilon(\pm R) = \mp \frac{1}{\sqrt{\omega - 1}}. \qquad (4.23)$$

Therefore if $\omega > 1$ the droplet will have a tip angle Θ, with $\sin \Theta / 2 = 1/\sqrt{\omega}$. If $\omega \leq 1$, $\rho(\upsilon)$ (given by (4.22)) goes to zero only in the limit $\upsilon \to \infty$. If υ goes to infinity, the droplet is smooth since the tip angle is $\Theta = 180°$.

From

$$\frac{dz}{dv} = \frac{dz}{d\rho}\frac{d\rho}{dv} \tag{4.24}$$

with (4.22) and the definition of v we get

$$\frac{dz}{dv} = -r\frac{1}{v}\left(\frac{3v\left(1 - v^2(\omega - 1)\right)}{(v^2 + 1)^{5/2}} + \frac{2v(\omega - 1)}{(v^2 + 1)^{3/2}}\right) \tag{4.25}$$

Integrating both sides, with the condition $z(v = 0) = 0$, we arrive at

$$z(v) = -\frac{rv\left(v^2(\omega + 1) + 2\omega + 1\right)}{(v^2 + 1)^{3/2}} \tag{4.26}$$

This last step, together with (4.22), gives us a parametrization of the surface of the droplet through v. The possible shapes of the droplet for various ω are plotted in Figure 4.1.

Since we know that v is bounded by (4.23), $z(v(\pm R)) = \pm R$. If $\omega > 1$ then we can compute the aspect ratio α substituting (4.23) into (4.22) for $z = R$:

$$\alpha := \frac{R}{r} = 2\sqrt{\omega} \tag{4.27}$$

If $\omega \leq 1$, v goes from $-\infty$ to $+\infty$, and the aspect ratio is obtained by considering the limiting case $v \to \infty$ in (4.22):

$$\alpha := \frac{R}{r} = \omega + 1 \tag{4.28}$$

The aspect ratio is a continuous function of ω (Figure 4.2):

$$\alpha(\omega) = \begin{cases} 2\sqrt{\omega} & \omega > 1 \\ 1 + \omega & \omega \leq 1 \end{cases} \tag{4.29}$$

Figure 4.2: Aspect ratio and tip angle in function of the anchoring strenght ω.
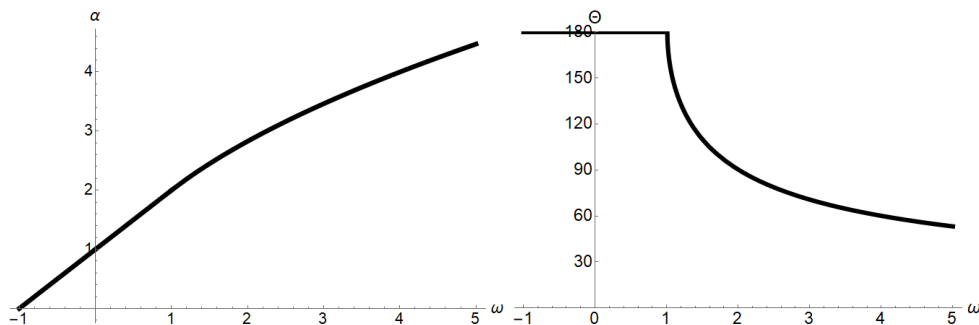
It is important to notice that the droplet will be oblate ($\alpha < 1$) only in case of homeotropic anchoring $\omega < 0$. Moreover, the aspect ratio and the tip angle are

not dependent on the size of the droplet, but only on the anchoring strength ω.

From (4.22) and (4.26) it is possible to calculate the volume of the droplet. A solid of revolution has a volume of

$$V = \pi \int_R^R \rho^2(z)dz = \pi \int \rho^2(z(v))\frac{dz}{dv}dv \qquad (4.30)$$

which becomes

$$V = r^3 \begin{cases} \frac{32}{105}\pi(1/\sqrt{\omega} + 7\sqrt{\omega}) & \omega > 1 \\ \frac{4}{105}\pi(\omega^3 - 7\omega^2 + 35\omega + 35) & -1 \le \omega \le 1 \end{cases} \qquad (4.31)$$

We can also compute the value of the free energy from (4.16):

$$F(\omega, r) = \gamma r^2 \begin{cases} \frac{32}{35}\pi(1/\sqrt{\omega} + 7\sqrt{\omega}) & \omega > 1 \\ 4\pi\left(\frac{1}{35}\omega((\omega - 7)\omega + 35) + 1\right) & -1 \le \omega \le 1 \end{cases} \qquad (4.32)$$

The volume is the variable we are interested in, the next step is solving for r and substituting in (4.32).

$$F(\omega, V) = \gamma V^{2/3} \begin{cases} 2\,6^{2/3}\left(\frac{\pi}{35}(7\sqrt{\omega} + 1/\sqrt{\omega})\right)^{1/3} & \omega > 1 \\ 6^{2/3}\left(\frac{\pi}{35}\omega((\omega - 7)\omega + 35) + 1\right)^{1/3} & -1 \le \omega \le 1 \end{cases} \qquad (4.33)$$
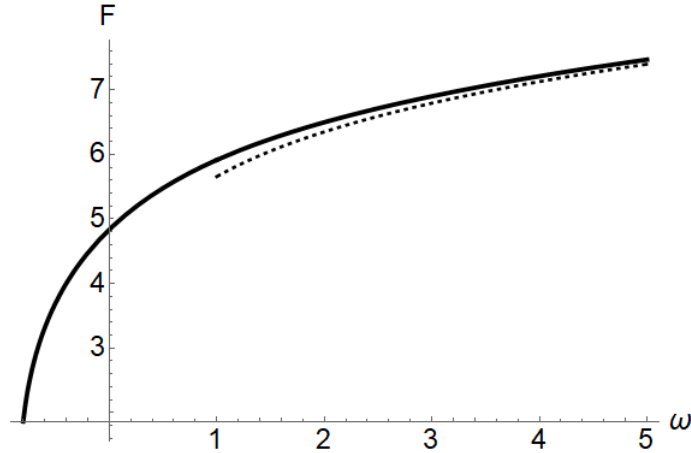

Figure 4.3: Plot of F in function of ω (solid), expansion around $\omega = \infty$ (dashed).

By expanding (4.33) in series around $\omega = +\infty$ we get

$$F(\omega, V) = \gamma V^{2/3}\,2\,6^{2/3}\left(\frac{\pi}{5}\right)^{1/3}\omega^{1/6} + O\left(\omega^{5/6}\right) \qquad (4.34)$$

at $\omega = 2$ there is only a 1% error between the exact formula and the limit.

Given equations (4.22) and (4.26), we can take the limit $\omega \to \infty$, taking into account that also $v \in [-1/\sqrt{\omega - 1}, 1/\sqrt{\omega - 1}]$, we get

$$\rho(v) = r(1 - v^2) \qquad z(v) = -2rv\sqrt{w} \qquad (4.35)$$

4.3   The elliptic lemon coordinates

In this section we introduce the elliptic lemon, which can be seen as an extension of the lemon coordinates [35]. The coordinates are the following

$$x = \frac{R}{e\sqrt{1-c^2}}(\sin v - c)\cos u$$

$$y = \frac{R}{e\sqrt{1-c^2}}(\sin v - c)\sin u \qquad (4.36)$$

$$z = \frac{R}{\sqrt{1-c^2}}\cos v$$

where R and $e > 0$ are parameters, while $0 \leq c \leq 1$, $\arcsin(c) \leq v \leq \pi - \arcsin(c)$, and $0 \leq u < 2\pi$ are the coordinates. The angle ϕ gives the angle between the x axis and the projection of the position vector on the xy-plane. Taking advantage of the revolution symmetry around the z axis, in Figure 4.4 are plotted various curves at fixed v(solid) and fixed c (dashed). The foci of the coordinates are located at $z = \pm R$.
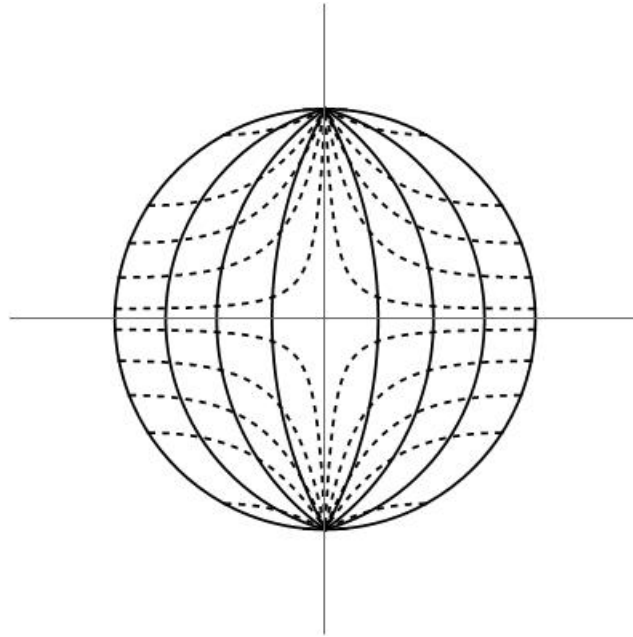
Figure 4.4: Coordinates curves for v (solid) and c (dashed).

By fixing $c = c_0$ we obtain a two-dimensional revolution surface parametrized by ϕ and v, with two important features: The major axis has length corresponding to R, while the minor axis r is

$$r = \frac{R}{e}\sqrt{\frac{1-c_0}{1+c_0}}. \qquad (4.37)$$

Thus, we can compute the aspect ratio of the shape

$$\alpha = \frac{R}{r} = e\sqrt{\frac{1+c_0}{1-c_0}} \qquad (4.38)$$

The surface has a tip angle Θ given by

$$\cos(\Theta/2) = c_0 \tag{4.39}$$

This implies that through e and c_0 we are able to modify the aspect ratio and the tip angle independently.

The special cases are given by $c = 0$, where the surface is an ellipsoid of aspect ratio $\alpha = e$; and $e = 1$, where the surface is given by the intersection of two circles.

The surface can also be expressed in implicit form as follows

$$z^2 = R^2 - 2c\,eR\frac{\rho}{\sqrt{1-c^2}} - e^2\rho^2 \tag{4.40}$$

or

$$\rho = \frac{R}{e\sqrt{1-c^2}}\left(\sqrt{1-(1-c^2)\frac{z^2}{R^2}} - c\right) \tag{4.41}$$

where $\rho = \sqrt{x^2+y^2}$.

We can compute the volume by integrating the surface and we get

$$V = \frac{2\pi R^3\left(c^2 - 6c\frac{\arccos(c)}{\sqrt{1-c^2}} + 2\right)}{3\left(1-c^2\right)e^2} \tag{4.42}$$

which can be inverted to get the major axis R as a function of the volume

$$R = \sqrt[3]{\frac{3V\left(1-c^2\right)e^2}{2\pi\left(c^2 - 6c\frac{\arccos(c)}{\sqrt{1-c^2}} + 2\right)}}. \tag{4.43}$$
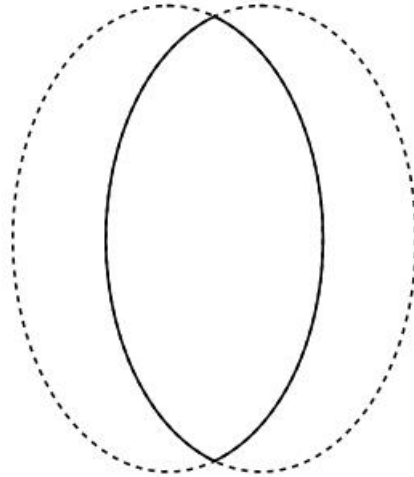
Figure 4.5: The revolution surface (solid), seen as an intersection of two ellipses (dashed).

The three-dimensional surface can be seen as the intersection of two ellipses of aspect ratio e, and small radii $r_{ell} := R/\sqrt{1-c^2}$ separated by a distance $r_{ell}\,c$.

If we take the elliptic-lemon surface and impose the constraints

$$\alpha = 2\sqrt{\omega} \qquad \sin\Theta/2 = \omega^{-1/2}, \tag{4.44}$$

we get

$$c = \sqrt{\frac{\omega - 1}{\omega}} \qquad e = 2(\omega - \sqrt{\omega}\sqrt{\omega - 1}) \tag{4.45}$$

in this case, $\rho(z)$ is given by

$$\rho(z) = \sqrt{4r^2\omega^2 - z^2} - 2r\sqrt{(\omega - 1)\omega} \tag{4.46}$$

where $r := R/2\sqrt{\omega}$, is the minor axis. Given $\rho(z)$, we can compute $v := \frac{d\rho}{dz}$ and invert it to express ρ and z as a function of v. The result is

$$\rho(v) = -2r\left(\sqrt{(\omega - 1)\,\omega} - \frac{\omega}{\sqrt{v^2 + 1}}\right) \qquad z(v) = -\frac{2\,r\,v\,\omega}{\sqrt{v^2 + 1}} \tag{4.47}$$

Expanding in series for $\omega = +\infty$ we get

$$\rho(v) = r(1 - v^2) \qquad z(v) = -2rv\sqrt{w} \tag{4.48}$$

that is exactly the same result as (4.35). Therefore the shape given by the Wullf's construnction for $\omega \to +\infty$ is the intersection of two ellipses. This approximation is sufficiently good for $\omega > 1.8$.

5. Bipolar droplets

In this chapter we introduce one model to explain the first transition, namely the one between homogeneous and bipolar droplets. This transition has been explained by Williams in [18] and clarified by Prinsen and Van Der Schoot in [3] and [36]. In the following, we expand the model developed by Prinsen and Van Der Schoot in [36], adapting it to the shape described in the previous chapter.

5.1   The shape of the droplet

We use the elliptic lemon coordinates (Section 4.3) to parametrize the shape of our droplet. We have the surface parametrized by v and u with R, c, e as constants. These parameters allow us to change the volume, the aspect ratio and the tip angle independently. The main difference with the work done in [36] is in the parameter e. In that case aspect ratio and tip angle were constrained, since $e = 1$. The addition of this last parameter allow us to increase the degrees of freedom of the surface.
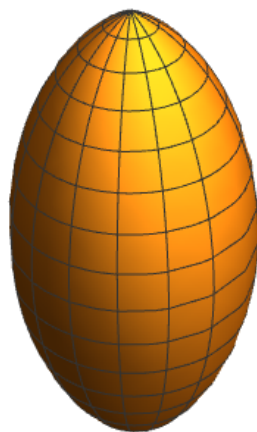

Figure 5.1: Example of the three-dimensional droplet for $e = 1.5$ and $c_0 = 0.3$.

We are interested not only on the surface, but also on the volume bounded by it. The coordinates in equation (4.36) can also be used to this aim, by fixing the minimum value for c to c_0, and including c in the coordinates, i.e. (c,v,u). For $c_0 = 0$ we get a sphere (or ellipsoid); by shifting the minimum value to c_0, we can get a solid with a fixed tip angle ($\cos \Theta/2 = c_0$). In this case c_0, e and R are the constants that define the shape of the droplet.

5.2   The director field

From the work of Van Der Schoot and Prinsen [36], we know that the nematic field of a bipolar droplet is always tangent to its surface and joining one pole to the other. On the inside, the lines of the nematic field also join one pole with the other, as shown in Figure 5.2. In the coordinates above, the nematic
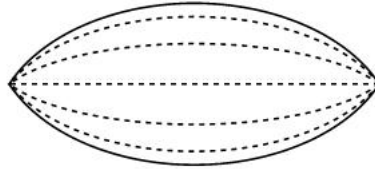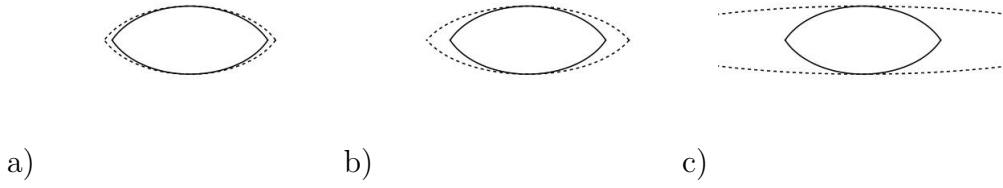

Figure 5.2: Section of the bipolar droplet (solid) with the nematic field lines (dashed).

field is given by e_v, the unit vector tangent to the coordinate curve of v. The next step is to build a nematic field dependent on a parameter that allows us to pass continuously from a bipolar to a homogeneous nematic field. We define a second set of coordinates given by the elliptic lemon coordinates, expanding the z coordinate by a factor $\beta \geq 1$:

$$
\begin{aligned}
x &= \frac{R}{e\sqrt{1-c'^2}}(\sin v' - c')\cos u' \\
y &= \frac{R}{e\sqrt{1-c'^2}}(\sin v' - c')\sin u' \\
z &= \frac{\beta R}{\sqrt{1-c'^2}}\cos v'
\end{aligned}
\tag{5.1}
$$

where R and e are the same as above. In Figure 5.3 are shown the droplet (solid) and the shape given by (5.1)(dashed) for different values of β.

In Figure 5.4 we plot the nematic field $n = e_{v'}$, given by the unit vector tangent to the coordinate curves of v'.

Figure 5.3: Section of the bipolar droplet (solid), and shape of the expanded coordinates (dashed) for $\beta = 1.1(a), 1.3(b), 3(c)$.
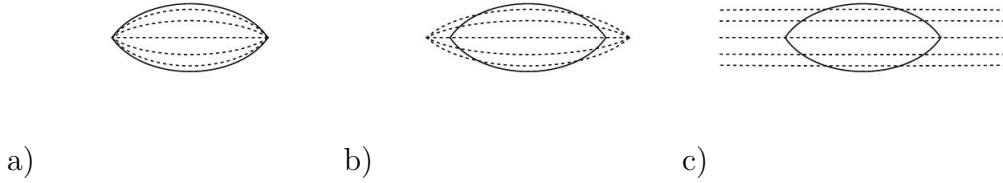
Figure 5.4: Bipolar droplet (solid), trajectories of n (dashed) with $\beta = 1(a), 1.3(b), 10(c)$.

In the case $\beta = 1$, we get the same result of Figure 5.2, while for $\beta > 1$ the poles of the vector field are located outside the droplet and at $\beta = \infty$ we get a homogeneous vector field.

With this construction, through the parameter β we are able to change the nematic field from bipolar to homogeneous.

The next step is to compute the Frank-Oseen energy. The bulk energy densities depend on the following terms, expressed in the (c', v', u') coordinates:

$$\nabla \cdot n = \frac{2\sqrt{1 - c'^2}e\left(1 - \beta^2 e^2\right)\sin(2v')}{R\left(\beta^2 e^2 + (1 - \beta^2 e^2)\cos(2v') + 1\right)^{3/2}} \tag{5.2}$$

$$\|\nabla \times n \times n\|^2 = \frac{8\beta^2\left(1 - c'^2\right)e^4}{R^2\left(\beta^2 e^2 + (1 - \beta^2 e^2)\cos(2v') + 1\right)^3} \tag{5.3}$$

$$\nabla \times n \cdot n = 0 \tag{5.4}$$

Leaving out the saddle-splay term, the total free energy is

$$F = \int_{\mathcal{B}} K_1(\nabla \cdot n)^2 + K_3\|\nabla \times n \times n\|^2 \, dV + \gamma \int_{\partial\mathcal{B}} 1 + \omega(n \cdot \nu)^2 dS \tag{5.5}$$

Since we want to minimize F at constant volume, we can employ equation (4.43), thus we can rewrite the three terms as follows

$$K_1 \int_{\mathcal{B}} (\nabla \cdot n)^2 dV =: K_1 V^{1/3} Y \tag{5.6}$$

$$K_3 \int_{\mathcal{B}} \|\nabla \times n \times n\|^2 \, dV =: K_3 V^{1/3} B \tag{5.7}$$

$$\gamma \int_{\partial \mathcal{B}} dS =: \gamma V^{2/3} S \tag{5.8}$$

$$\gamma \omega \int_{\partial \mathcal{B}} (n \cdot \nu)^2 dS =: \gamma \omega V^{2/3} A \tag{5.9}$$

where Y, B, S, A are the integrals independent of V. Let $\kappa := K_1/K_3$, we can write

$$F = K_3 V^{1/3}(B + \kappa Y) + \gamma V^{2/3}(S + \omega A) \tag{5.10}$$

To carry out the minimization we compute the various integrals B, Y, S and A numerically for various β, c_0 and e. Minimizing F at a constant volume is equivalent to minimizing $\tilde{F}$ defined as

$$\tilde{F} = (B + \kappa Y) + \lambda(S + \omega A) \tag{5.11}$$

at constant λ, where $\lambda := \frac{\gamma V^{1/3}}{K_3}$.

From [2] and [15], we set $\kappa = 1$ and $\omega = 2$, and proceed to numerically minimize $\tilde{F}$. We compute the energy terms for various configurations given by e, c_0 and β and weight them with λ, where λ goes from 10^{-3} to 10^3. Instead of c_0 and e consider for representation the aspect ratio α and tip angle Θ (in degrees), where

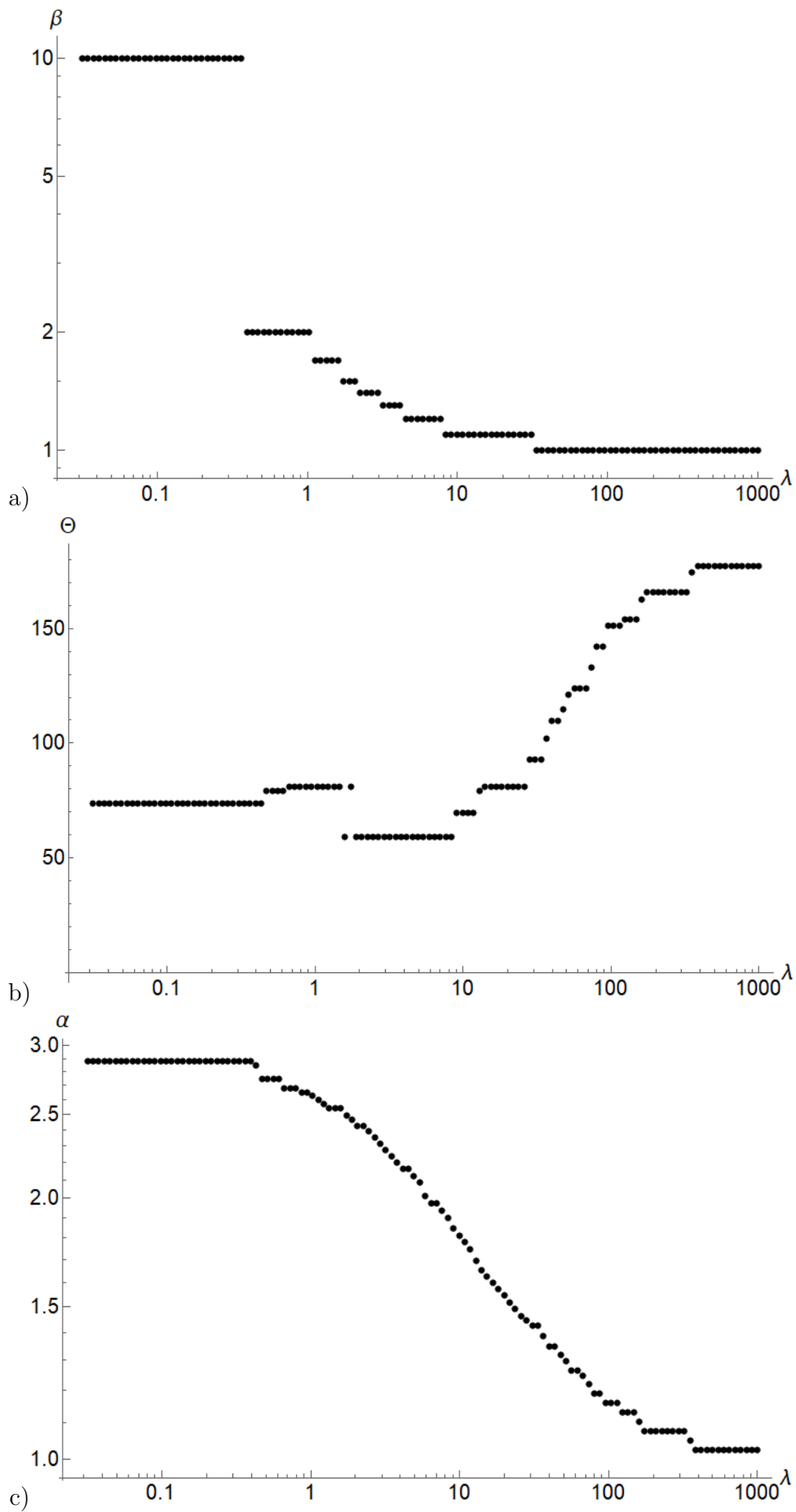$$\Theta = \frac{360}{\pi} \arccos(c_0) \qquad \alpha = e \sqrt{\frac{1 + c_0}{1 - c_0}}, \tag{5.12}$$

In Figure 5.5 we plot the values of Θ as a function of α for various λ.
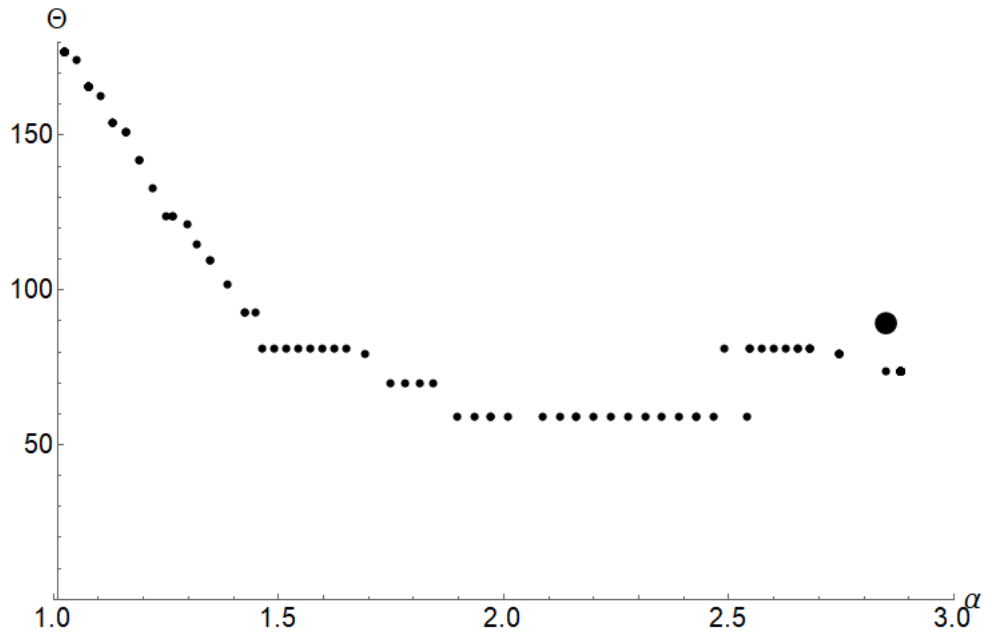
Figure 5.5: Path in the Θ, α space of the minimum of the energy. For $\omega = 2$ and $\kappa = 1$. The big black circle represents the Wulff's construction.

In Figure 5.6 are shown the behaviour of the three quantities as a function of λ. Since $\lambda \propto V^{1/3}$ a small lambda implies a small volume.

Figure 5.6: Plot of β (a), Θ(b) and α(c) as a function of λ.

We see that when $\lambda \to 0$, α and Θ tend to the value given by the Wulff's construction, represented as a black dot in Figure 5.5. The numerical analysis does not converge exactly to the value given by the construction, where for $\omega = 2$, $\alpha \approx 2.8$ and $\Theta = 90°$. The difference may be due to the fact that the shape we are using is not exactly the Wulff's shape, but an approximation for large ω; moreover, the nematic field is not exactly homogeneous since $\beta = 10$.

As the volume increases, when $\lambda \approx 1$ the aspect ratio begins to decrease monotonically, to finally converge to 1 for large volumes. The same happens for β, the parameter that modifies the nematic field. Therefore, the poles of the nematic field get closer to the poles of the droplet. When $\beta = 1$ the nematic field is exactly bipolar.

The behaviour of Θ is not monotonous. It starts from 74° and grows. At $\lambda \approx 1$ the value drops quite sharply to 60° and then grows monotonically to 180°.

For large volumes, when $\lambda \to +\infty$, the shape is a sphere: $\alpha = 1$ and $\Theta = 180°$. The nematic field is perfectly bipolar, in fact $\beta = 1$.

5.2.1   Comparison with experimental data

In Figure 5.7, we plot the result of the numerical analysis with the data from [15].
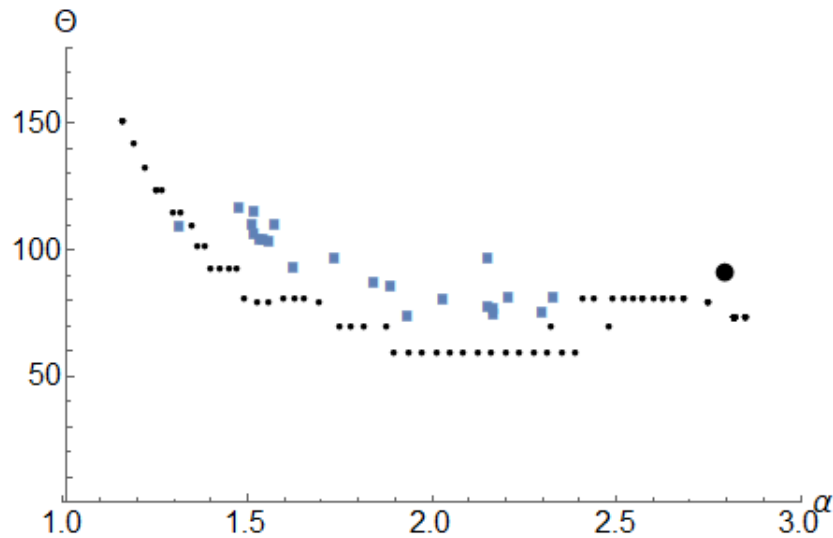
Figure 5.7: Result of the theory (black) with the data (blue).

While being close to the experimental data, the theory with the given parameters systematically underestimates Θ for any α. We know that the theoretical curve depends only on the two parameters κ and ω. By numerical inspection, we see that the theoretical prediction is not affected by the value of κ, while it depends mainly on ω.
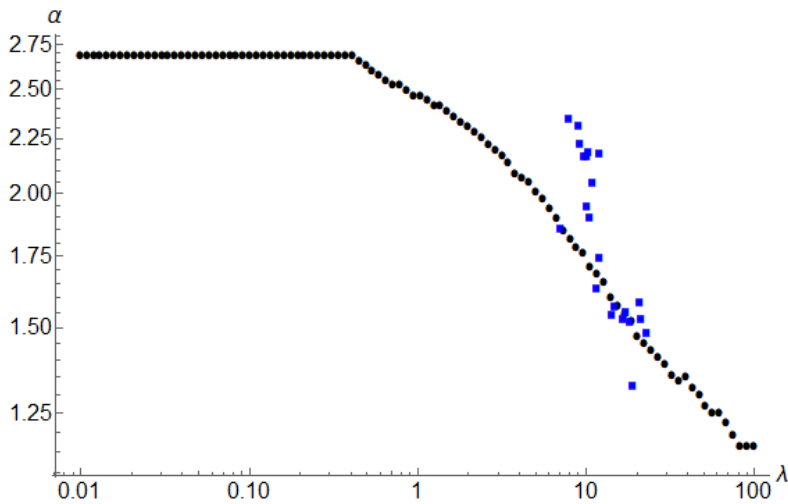
The best fit is given by $\omega = 1.7$. In Figure 5.8 we plotted the result for that
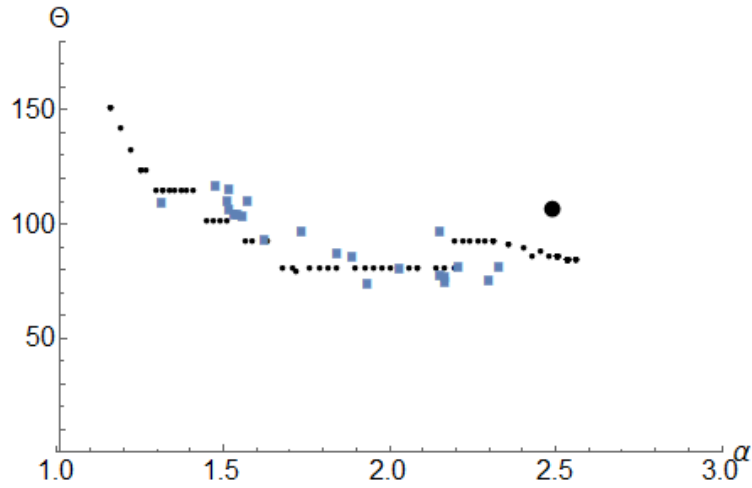
Figure 5.8: Result of the theory (black) for $\omega = 1.7$, with the data (blue).

value of ω and $\kappa = 1$. The analysis done in the previous paragraph remains the same qualitatively.

Figure 5.9 and Figure 5.10 show the aspect ratio and tip angle as a function of λ for the theory and from the data.

Figure 5.9: Aspect ratio as function of λ: theory (black) for $\omega = 1.7$, with the data (blue).

The ratio K/λ necessary to compute λ has be choosen to best fit the data. In this case $K/\lambda = 15\,\mu m$, larger than the one estimated in [2] by a factor of 15.

In Figure 5.9 the aspect ratio is plotted in function of λ. In both cases, the aspect ratio decreases with increasing volume, but with different slopes. The disagreement may be due to errors in the measurements or to an error in the estimate of the ratio K/γ. By changing that ratio, the data set gets shifted on the the λ axis but does not change the slope of the set.

In Figure 5.10 the tip angle Θ is plotted per different volumes. For $K/\gamma = 1$ and $\omega = 1.7$. The agreement is quite nice, although a slight deviation is visible.
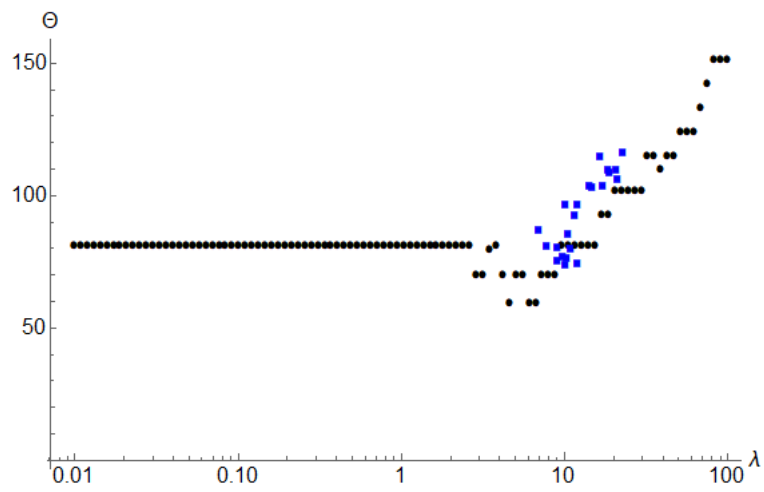
Figure 5.10: Tip angle as function of λ: theory (black) for $\omega = 1.7$, with the data (blue).

6.   Confined twisted field

In this chapter we introduce a first model that takes into account the twist. This will serve as a blueprint for the next chapter. Here we consider a nematic field with only the twist energy term in the bulk energy.

6.1   The nematic field

In this chapter we want to study the case of a twisted nematic field

$$n = \cos(qx_3 + \phi)e_1 + \sin(qx_3 + \phi)e_2 \tag{6.1}$$

under confinement.

For simplicity, we will consider an elliptic droplet with aspect ratio α, whose axis is directed along e_z. This means that the surface is described by the equation (Figure 6.1)

$$x^2 + y^2 + \frac{z^2}{\alpha^2} = r^2 \tag{6.2}$$

where $r := \left(\frac{3V}{4\pi\alpha}\right)^{1/3}$ and V is the volume of the ellipsoid, which will be treated as a constant of the droplet.
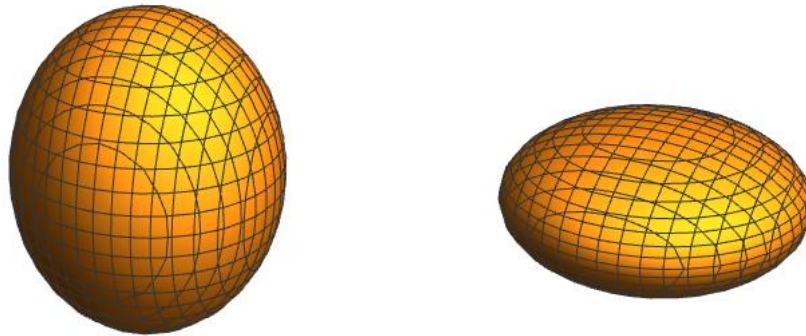
a)   b)

Figure 6.1: Surface of a prolate ellipsoid with $\alpha = 1.5$, and of an oblate ellipsoid with $\alpha = 0.5$.

6.2   Case 1: Parallel axes

In this case we allineate the cholesteric axis with the revolution axis of the ellipsoid. the director field is

$$n = \cos(qz + \phi)e_x + \sin(qz + \phi)e_y \tag{6.3}$$

Plugging this formula into eq. (3.23), the bulk energy is simply given by

$$F_B = K_2(q - q_\infty)^2 V \tag{6.4}$$

as shown in the previous chapter, independent of α and ϕ.

The surface energy can be computed as follows

$$F_S = \gamma \int_{\partial \mathbb{B}} \left(1 + \omega(n \cdot \nu)^2\right) dS. \tag{6.5}$$

By parametrizing the surface as $z = \pm \alpha r \sqrt{1 - \rho^2}$, we get $dS = \rho\sqrt{1 + \left(\frac{\partial z}{\partial \rho}\right)^2} d\rho du$, where $x = r\rho\cos(u)$ and $y = r\rho\sin(u)$. The scalar product becomes

$$(n \cdot \nu) = \frac{\cos(u)\cos(qz + \phi)\frac{\partial z}{\partial \rho} + \sin(u)\sin(qz + \phi)\frac{\partial z}{\partial \rho}}{\sqrt{1 + \left(\frac{\partial z}{\partial \rho}\right)^2}} \tag{6.6}$$

We can split the two contributes of (6.5) as

$$F_S = V^{2/3}\gamma(S + \omega A), \tag{6.7}$$

the isotropic surface tension is

$$S = 2\left(\frac{3}{4\pi\alpha}\right)^{2/3} \int_0^1 d\rho \int_0^{2\pi} du \rho^2 \sqrt{\frac{(\alpha^2 - 1)\rho^2 + 1}{1 - \rho^2}} \tag{6.8}$$

where the 2 comes from the fact that the integration is the same if carried out on the upper ($z > 0$) and lower ($z < 0$) half of the ellipsoid. Performing the integration, we obtain

$$S = 2\pi\left(\frac{3}{4\pi\alpha}\right)^{2/3} \left(\frac{\alpha^2 \log\left(\frac{\sqrt{1 - \alpha^2} + 1}{\alpha}\right)}{\sqrt{1 - \alpha^2}} + 1\right). \tag{6.9}$$

The anisotropic part has the form

$$A = A_+ + A_-, \tag{6.10}$$

where

$$A_{\pm} = \left(\frac{3}{4\pi\alpha}\right)^{2/3} \int_0^1 d\rho \int_0^{2\pi} du \frac{\alpha^2 \rho^3 \cos^2\left(\phi - u \pm \alpha q\sqrt{1 - \rho^2}\right)}{\sqrt{1 - \rho^2}\sqrt{(\alpha^2 - 1)\rho^2 + 1}} \tag{6.11}$$
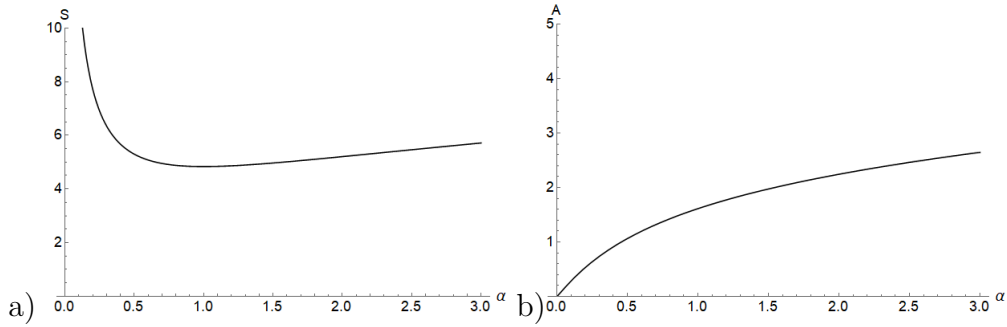
with + and - indicating the upper and lower half of the ellipsoid, respectively. In both cases, integrating over u from 0 to 2π gives

$$A_\pm = \left(\frac{3}{4\pi\alpha}\right)^{2/3} \int_0^1 d\rho \frac{\alpha^2\rho^3\pi}{\sqrt{1-\rho^2}\sqrt{(\alpha^2-1)\rho^2+1}} \tag{6.12}$$

The dependence on ϕ, q and z disappears, therefore $A_+ = A_-$ and $A = 2A_\pm$. Integrating on ρ we get

$$A = 2\pi \left(\frac{3}{4\pi\alpha}\right)^{2/3} \frac{\alpha^2}{4} \cdot \frac{\left(2-\alpha^2\right)\log\left(\frac{-\alpha^2+2\sqrt{1-\alpha^2}+2}{\alpha^2}\right) - 2\sqrt{1-\alpha^2}}{(1-\alpha^2)^{3/2}} \tag{6.13}$$

Equation (6.9) and (6.13) are plotted in Figure 6.2.

Figure 6.2: (a) Plot of $S(\alpha)$ and (b) plot of $A(\alpha)$.

The surface energy

$$F_S = \gamma V^{2/3} \left(S + \omega A\right) \tag{6.14}$$

does not depend on q or the phase ϕ. Therefore, the value of q is obtained by minimizing (6.4), i.e. $q = q_\infty$, while the aspect ratio is given by minimizing F_S. In Figure 6.3(a) F_S is plotted for various ω.

The α^* minimizing of F_S depends only on ω, and is shown in Figure 6.3(b). The favoured shape for positive anchoring strength is given by oblate ellipsoids.
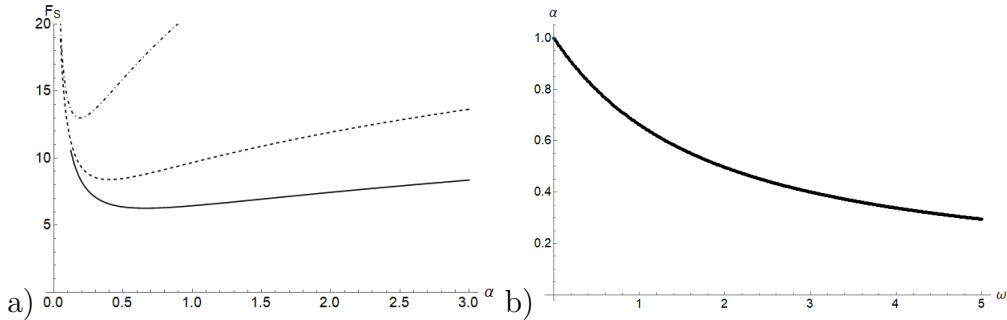
Figure 6.3: (a) Plot of $S + \omega A$ for $\omega = 1$ (solid), 3(dashed) and 10(dot-dashed); (b) Plot of $\alpha^*(\omega)$

Therefore, this simple model gives a constant natural twist q_∞ for every volume, with an aspect ratio only dependent on ω. The favourite shape is an oblate ellipsoid.

From the jones matrix calculus we can simulate the cross-polarized microscope with the parameters above and get the image reported in Figure 6.4.
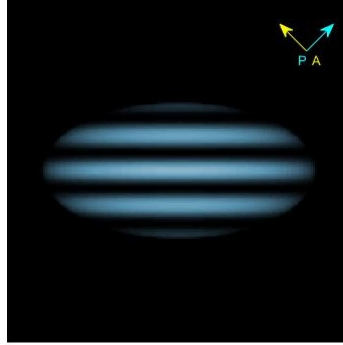

Figure 6.4: Simulation for $\alpha = 0.5$.

6.3   Case 2: Perpendicular axes

In this case we align the cholesteric axis perpendicularly to the revolution axis of the ellipsoid. Therefore we have

$$n = \cos(qx + \phi)e_z + \sin(qx + \phi)e_y \tag{6.15}$$

As in the previous case, the bulk energy remains (6.4) and $F_S = V^{2/3}\gamma(S+\omega A)$, with S as before. We want to compute the anchoring energy

$$A = A_+ + A_-, \tag{6.16}$$

also in this case $A_+ = A_-$, that is $A = 2A_\pm$:

$$A = 2\left(\frac{3}{4\pi\alpha}\right)^{2/3} \int\limits_0^1 d\rho \int\limits_0^{2\pi} du \; \rho \frac{\alpha^2\rho^2 \sin(u)^2 \sin^2(\phi + qr\rho\cos(u)) + (1-\rho^2)\cos^2(\phi + qr\rho\cos(u))}{\sqrt{1-\rho^2}\sqrt{(\alpha^2-1)\rho^2+1}} \tag{6.17}$$

It depends on q, r and α. We can rescale q as $\tilde{q} = qV^{1/3}$ and $\tilde{r} = r/V^{1/3} = \left(\frac{3}{4\pi\alpha}\right)^{1/3}$, so that the integral does not depend on V. The results for different values of α and ϕ are shown in Figure 6.5.

The resulting shape of A is Bessel-like, see Figure 6.6 . In the case of $\alpha > 1$ and $\phi < \frac{\pi}{4}$, $\tilde{q} = 0$ is a minimum, while is a maximum for $\phi > \frac{\pi}{4}$. Its global minimum (maximum) value is reached at $\phi = 0$ ($\phi = \pi/2$). The reverse is valid for $\alpha < 1$ where the minimum (maximum) is attained at $\phi = \frac{\pi}{2}$ ($\phi = 0$).
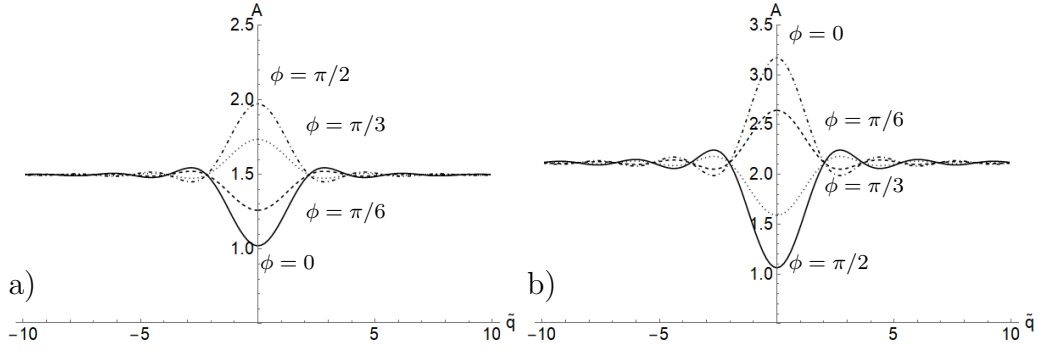
Figure 6.5: Plot of A for $\alpha = 1.5$(a) and $\alpha = 0.5$(b) for various values of $\phi = 0, \pi/6, \pi/3, \pi/2$.
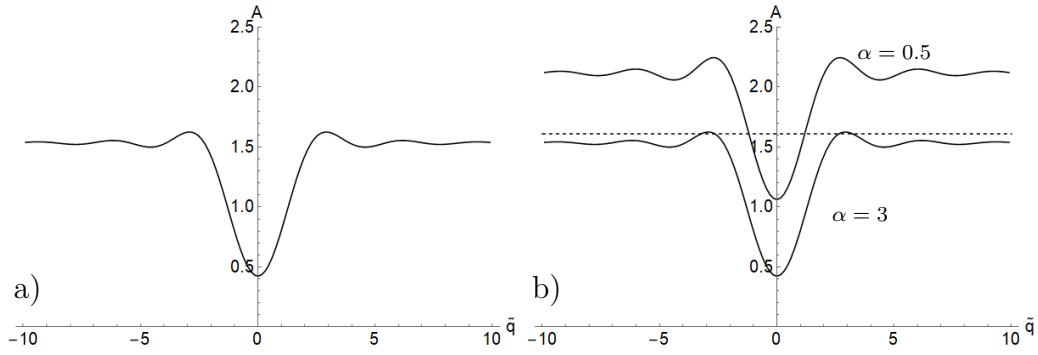
Figure 6.6: a) Plot of A for $\alpha = 3$, $\phi = 0$; (b) Plot of A for $\alpha = 3(\phi = 0)$, $\alpha = 0.5(\phi = \pi/2)$, and $\alpha = 1$ (dashed).

For any ϕ, A converges for $\tilde{q} \to \pm\infty$ to a value depending solely on α. Since we are interested in finding the minima, we will assume $\phi = \pi/2$ when $\alpha < 1$ and $\phi = 0$ when $\alpha > 1$.

For each α we can compute the value of A at $\tilde{q} = 0$ and at $\tilde{q} = \pm\infty$:

$$A_0 := \left(\frac{\pi}{2}\right)^{1/3} \left(\frac{3}{\alpha}\right)^{2/3} \begin{cases} \frac{1}{1-\alpha^2} + \frac{\alpha^2 \tan^{-1}\left(\sqrt{\alpha^2-1}\right)}{\left(\alpha^2-1\right)^{3/2}} & \alpha \geq 1 \\ \frac{\alpha^2\left(\sqrt{\alpha^2-1}+\left(\alpha^2-2\right)\tan^{-1}\left(\sqrt{\alpha^2-1}\right)\right)}{2\left(\alpha^2-1\right)^{3/2}} & \alpha < 1. \end{cases} \tag{6.18}$$

$$A_\infty := \frac{\pi}{2}\left(\frac{3}{4\pi\alpha}\right)^{2/3}\left(\frac{\alpha^2-2}{\alpha^2-1} + \frac{\alpha^4 \mathrm{atan}\left(\sqrt{\alpha^2-1}\right)}{\left(\alpha^2-1\right)^{3/2}}\right) \tag{6.19}$$

and plot the functions in Figure 6.7. From the graph we can see how the anchoring is minimized when the adimensional twist is zero, $\tilde{q} = 0$. Therefore the anchoring prefers an untwisted regime, where $qV^{1/3} \to 0$, rather than a fully twisted one.
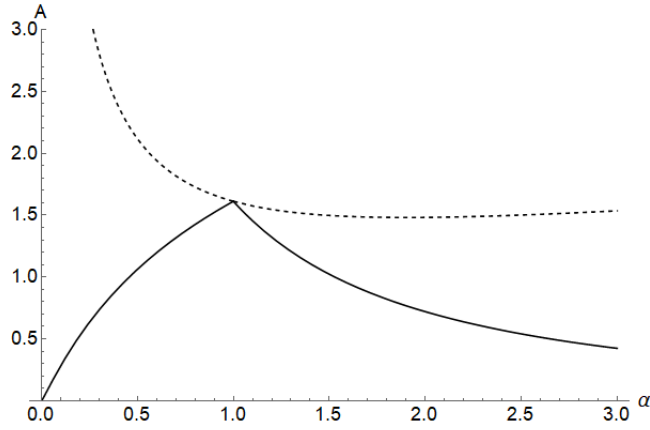
Figure 6.7: Plot of $A_0(\alpha)$ (solid), A_∞ (dashed).

Contrary to the parallel case, here we can distinguish two different behaviours. The two limiting behaviors correspond to $\tilde{q}_\infty \to 0$ and the second when $\tilde{q}_\infty \to \infty$. Indeed, the choice of the minimizing twist lies mainly on the bulk term, as its parabolic form diverges for values too far from q_∞, while in contrast A is always finite (see Figure 6.6).

If $\tilde{q}_\infty \to 0$, the anchoring strength does not depend on q. The twist term is minimized by the bulk energy, thus $q = q_\infty$ and A tends to A_0. The total energy, in this case, has the form

$$F = \gamma V^{2/3}(S + \omega A_0) \tag{6.20}$$

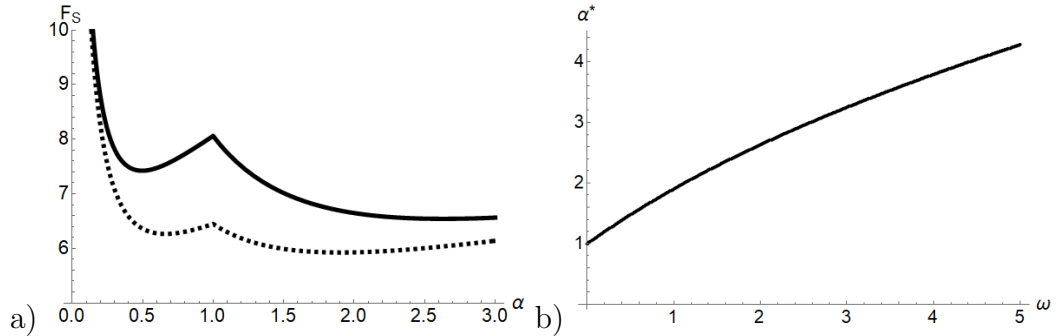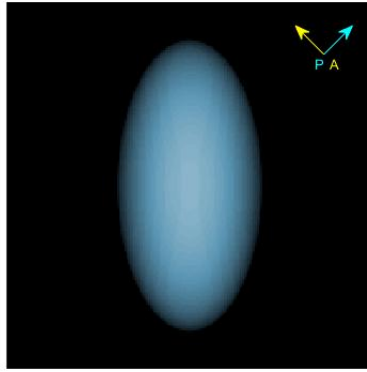It depends only on α, and it is plotted in Figure 6.8(a).

Figure 6.8: When $\tilde{q}_\infty \to 0$: Plot of F for $\omega = 1$ (solid) and $\omega = 2$ (dashed) (b); Plot of α^*.

We can minimize with respect to α and get the α^* that minimizes F_S for each ω (Figure 6.8(b)). In this case the prolate ellipsoid is favoured.

For $q = q_\infty$, $\tilde{q}_\infty \to 0$ implies that the radius of the droplet is much smaller than the natural pitch. This means that the droplet can be interpreted as being in the *homogeneous* case, where the nematic field is constant everywhere inside it. We can visualize the result in Figure 6.9.

If $\tilde{q}_\infty \to \infty$, then A tends to A_∞. As before the twist is minimized by $q = q_\infty$ and F has the form

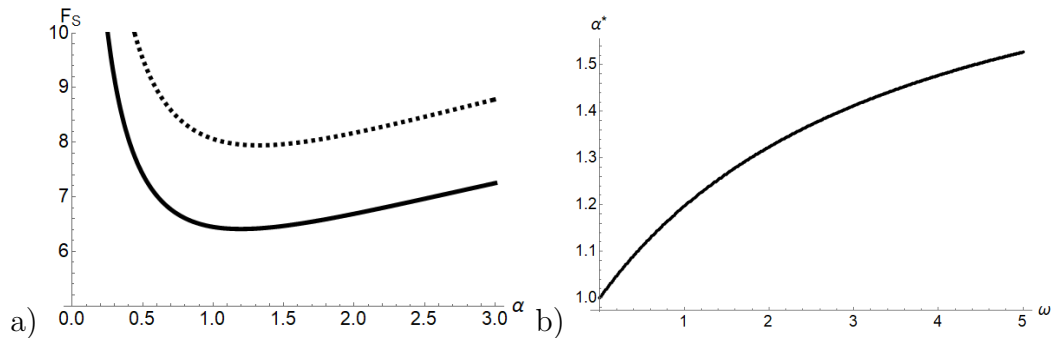$$F = \gamma V^{2/3}(S + \omega A_\infty) \tag{6.21}$$

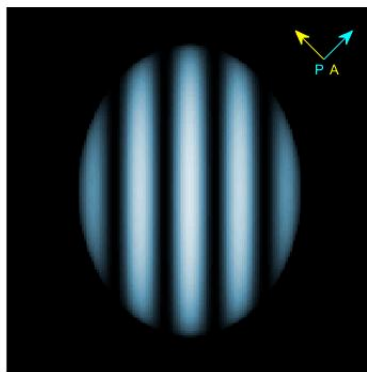**Figure 6.9:** Simulation for $\alpha = 2$ and $q_\infty V^{1/3} \to 0$.

The free energy depends only on α, and is plotted in Figure 6.10(a).

We can minimize respect to α and get the α^* in Figure 6.10(b).

Figure 6.10: For $\tilde{q}_\infty \to \infty$: Plot of F_S for $\omega = 1, 2$ and 5 (a); Plot of α^* (b).

Also in this case the prolate ellipsoid is favoured, while the pitch is minimized at its natural value. This case can be considered as the *cholesteric* phase, where birefringent bands form on the droplet, as shown in Figure 6.11.

Figure 6.11: Simulation for $\alpha = 2$ and $q_\infty V^{1/3} \to \infty$.

By comparing the aspect ratio of the two cases plotted in Figure 6.8(b) and
Figure 6.10(b), one can see that the equilibrium aspect ratio is larger for the
homogenous phase than for the cholesteric phase. This simple model gives a
transition between two different aspect ratios, depending on the volume.

When $\tilde{q}_\infty \sim 1$, the anchoring energy couples the aspect ratio α and the twist
q. The total energy is

$$F = K_2 V (q - q_\infty)^2 + V^{2/3} \gamma \left(S(\alpha) + \omega A(\alpha, qV^{1/3}) \right) \tag{6.22}$$
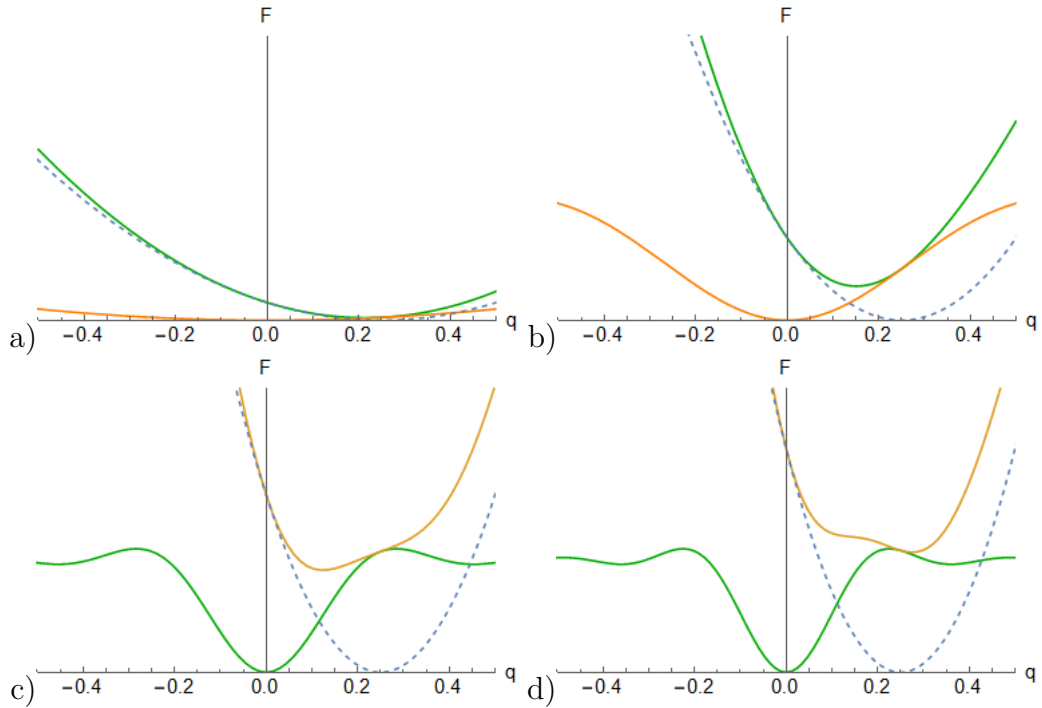
For simplicity, we limit the model to the case where $\alpha > 1$ is a constant. Thus,
we can drop the surface term from (6.22) to obtain

$$F = K_2 V (q - q_\infty)^2 + V^{2/3} \gamma \omega A(qV^{1/3}) \tag{6.23}$$

which can be rescaled as

$$\tilde{F} = \lambda V^{1/3} (q - q_\infty)^2 + A(qV^{1/3}) \tag{6.24}$$

where $\lambda := \frac{K_2}{\gamma \omega}$. The bulk term is a parabola centered in q_∞, while A is a
Bessel-like function as diplayed above. By fixing $\lambda = 1$ and $q_\infty = 0.25$ and by

Figure 6.12: Plot of $A(qV^{1/3})$ (green) and $V^{1/3}(q - q_\infty)^2$ (dashed blue) and their sum (orange) as a function of q for $V = 1(a), 100(b), 1\,000(c), 10\,000(d)$.

changing the volume, we plot the various results in Figure 6.12. In the first
plot (a), at a very small volume the energy has a minimum for $q = q_\infty$. As the
volume increases, the overall shape of A contracts proportionally to $V^{1/3}$ and
begins to shift the minimum towards a smaller q, i.e. a longer pitch $p > p_\infty$.
For even larger volumes the anchoring reaches the plateau given by A_∞, and

the parabola of the twist energy shrinks and brings the twist to its natural value q_∞.

To get an estimate of the transition volume, guided by (6.12)(c), we see that at the transition, the difference between the minimum (A_0) and the plateau value (A_∞) for the anchoring energy is roughly equal to the energy of the untwisted $(q = 0)$ cholesteric, namely

$$V^{2/3}\gamma\omega(A_\infty - A_0) = VK_2q_\infty^2 \tag{6.25}$$

by letting $\Delta := A_\infty - A_0$ we get the transition volume from the homogenous to the cholesteric phase:

$$V_{h\to c} = \left(\frac{\gamma\omega\Delta}{K_2q_\infty^2}\right)^3 \tag{6.26}$$

The quantity Δ is in of the order of the unity for $\alpha > 1$, as shown in Figure 6.13.
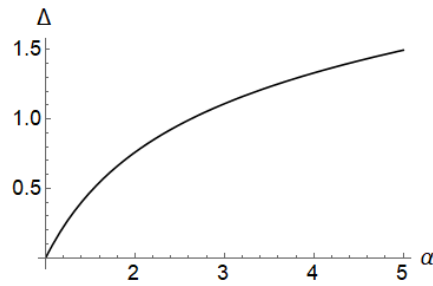

Figure 6.13: Plot of $\Delta = A_\infty - A_0$.

The model presented above displays two different phases that we called *homogeneous* and *cholesterics*. The phase change is driven by the volume, where we observe a change in aspect ratio. The critical volume for the transition has been estimated to be as in equation (6.26).

If we compare the two cases, the parallel axes case and the perperdicular axes case, when $V^{1/3}q \to 0$, the bulk energy is always minimized, while F_S depends solely on α as shown in Figure 6.14(a). The energy value for the prolate in the perpendicular axis is lower, thus for small volumes this configuration is preferred.
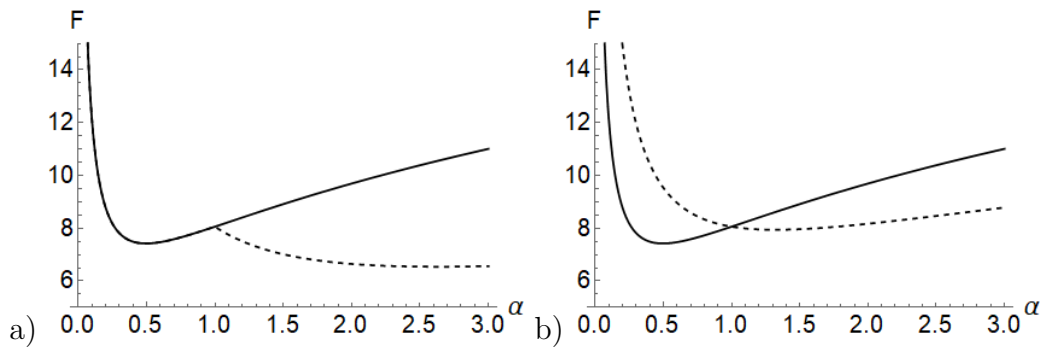

Figure 6.14: Plot of F_S for the perpendicular axis case (dashed) the parallel axis case (solid), when $\omega = 2$ as a function of α.

When $V^{1/3}q \rightarrow \infty$, the bulk energy is also minimized and in this case F_S is shown in Figure 6.14(b). The energy value for the oblate in the parallel axis case is lower, thus for larger volumes this configuration is preferred.

As explained in Chapter 2, the shape of the cholesterics droplets has been shown to be a prolate ellipsoid, thus this model is not able to predict the correct shape of the observed droplets.

In the following chapter we expand these models, in attempt to get the whole phenomenology in a unified model.

7. Cholesterics and onions

In this chapter we introduce a model capable of describing the whole phenomenology of the droplets described in chapter 2.

7.1 Oblate spheroidal coordinates

At first, we introduce the *oblate spheroidal coordinates*, from [37].

$$
\begin{aligned}
x &= \beta\sigma\tau \\
y &= \beta\sqrt{1+\sigma^2}\sqrt{1-\tau^2}\cos u \\
z &= \beta\sqrt{1+\sigma^2}\sqrt{1-\tau^2}\sin u
\end{aligned}
\tag{7.1}
$$

where $\sigma \in \mathbb{R}$, $0 \le \tau \le 1$ and $0 \le u < 2\pi$, while $\beta > 0$ is a parameter. If we look at the the coordinate curves in the plane x, y, we obtain the coordinate curves shown Figure 7.1, where the foci of the dashed ellipses are located at $(0, \pm\beta)$.
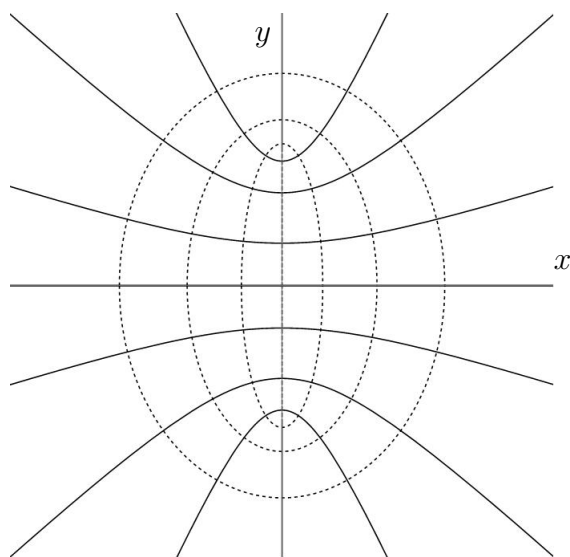
Figure 7.1: Coordinates curves for τ (solid) and σ (dashed). The 3D view is given by a revolution around the x-axis.

We define the following quantities to simplify the notation:

$$S_1 := \sqrt{1 - \tau^2}, \qquad S_2 := \sqrt{\sigma^2 + \tau^2}, \qquad S_3 := \sqrt{1 + \sigma^2} \qquad (7.2)$$

The metric induced by the coordinates is diagonal:

$$g = \begin{pmatrix} h_\sigma^2 & 0 & 0 \\ 0 & h_u^2 & 0 \\ 0 & 0 & h_\tau^2 \end{pmatrix} \qquad (7.3)$$

where $h_\sigma = \beta \frac{S_2}{S_3}$, $h_u = \beta S_1 S_3$ and $h_\tau = \beta \frac{S_2}{S_1}$. As a consequence the three unit vectors e_σ, e_u, e_τ form an orthonormal basis.

7.2   The nematic field

The nematic field introduced here is parametrized by spheroidal coordinates. We suppose that in the disk $y^2 + z^2 < \beta^2$ at $x = 0$ the nematic field is directed along the z-axis, that is $n = e_z$, see Figure 7.2(a), or in the new coordinates

$$n_1 = \cos(u)e_u - \sin(u)e_\tau \qquad (7.4)$$

while we define $n_2 = -\sin(u)e_u - \cos(u)e_\tau$ as the vector perpendicular to n_1.
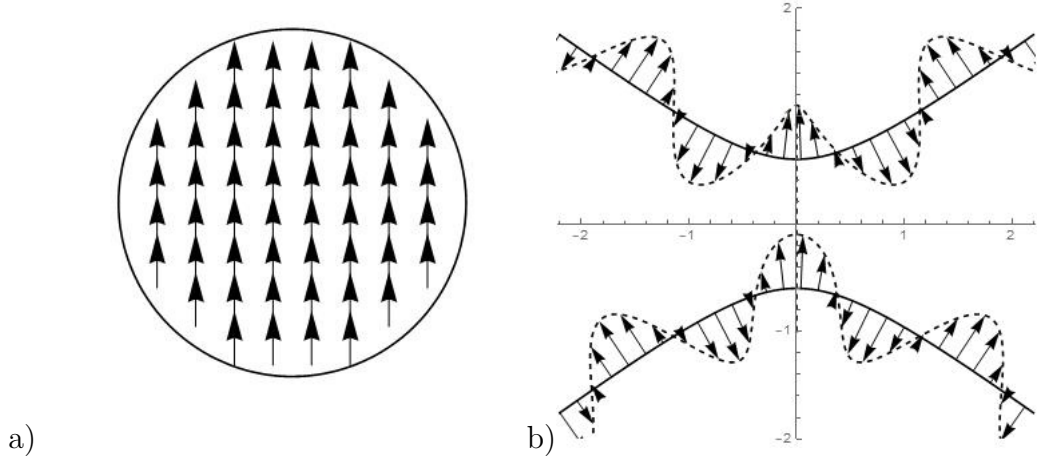
Figure 7.2: (a) Nematic field inside the disk $y^2 + z^2 < \beta^2$ at $x = 0$. (b) The cholesterics axis (solid) with the nematic field (arrows) for $\beta = 1$ at $y = 0$.

We want to use the coordinate curves of σ as the axes for our model. Therefore by Levi-Civita parallel transport, we transport n_1 and n_2, along the coordinate curves of σ. Since the coordinates are orthonormal and the parallel transport is a linear map, when applied on n_1 and n_2 along a coordinate curve gives back, respectively, n_1 and n_2. The nematic field is built by implementing an helix between n_1 and n_2 depending on $\beta\sigma$, such that for $x = 0$ (i.e. $\sigma = 0$), we get $n = n_1$. So we obtain

$$n = \cos(q\beta\sigma)n_1 + \sin(q\beta\sigma)n_2 \qquad (7.5)$$

which becomes

$$n = \cos(q\beta\sigma + u)e_u - \sin(q\beta\sigma + u)e_\sigma \tag{7.6}$$

where q is the wave number of the helix.

7.3 The parameter β

Before discussing the energy given by the nematic field we analyse the behaviour for different values of β.

The coordinates (7.1) can be inverted to express σ, τ and u as a function of x, y, z and β. If we take the limit for $\beta \to \infty$ we obtain

$$\sigma = x/\beta \qquad \tau = 1 \qquad u = \arctan 2(y, x) \tag{7.7}$$

which substituted into (7.6) gives

$$n = \cos(qx)e_z + \sin(qx)e_y. \tag{7.8}$$

Therefore the nematic field becomes a cholesteric with the axis given by e_x, and twist given by q. In Figure 7.3(a) the cholesteric axes are plotted.

In the limit $\beta \to 0$, σ becomes

$$\sigma = \frac{\text{sgn}(x)\sqrt{x^2 + y^2 + z^2}}{\beta} \tag{7.9}$$

and the nematic field has the axes divergent from the origin, which is better express in spherical coordinates (r, θ, ϕ) aligned with the x-axes:

$$n = \cos(qr)e_u + \sin(qr)e_\theta. \tag{7.10}$$

the result is also shown in Figure 7.3(c).
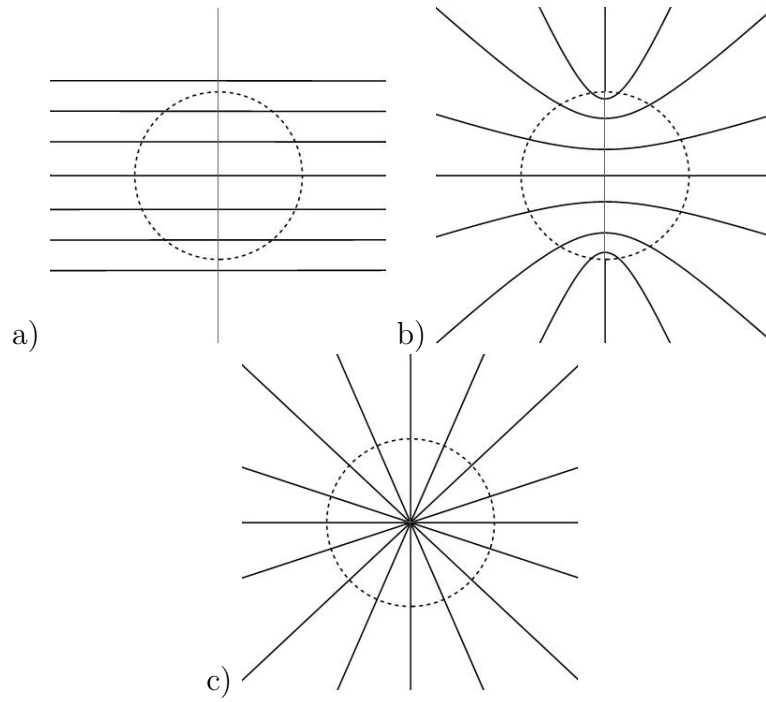
7.4 The Frank-Oseen energy

Given the nematic field as in equation (7.6) we compute the various terms of the Frank-Oseen energy.

$$\nabla \cdot n = \frac{\sin(q\beta\sigma + u)}{\beta S_1} \left(\frac{\tau \left(\sigma^2 + 2\tau^2 - 1\right)}{S_2^3} - \frac{1}{S_3} \right) \tag{7.11}$$

$$(\nabla \times n)_\sigma = \frac{\cos(\beta q\sigma + u)}{\beta} \frac{(\tau S_3 - S_2)}{S_1 S_2 S_3} \tag{7.12}$$

$$(\nabla \times n)_u = \frac{\sin(\beta q\sigma + u)}{\beta} \frac{\sigma S_3}{S_2^3} + q\cos(\beta q\sigma + u)\frac{S_3}{S_2} \tag{7.13}$$

$$(\nabla \times n)_\tau = \frac{\cos(\beta q\sigma + u)}{\beta} \frac{\sigma}{S_2 S_3} - q\sin(\beta q\sigma + u)\frac{S_3}{S_2} \tag{7.14}$$

Figure 7.3: Cholesterics axes plotted for different values of β : $(a) = 100, (b) = 1, (c) = 0.01$. As a reference, a circle of unitary radius is plotted.

$$\nabla \times n \cdot n = q\frac{S_3}{S_2} + \frac{\sin(2(\beta q\sigma + u))}{\beta}\frac{\sigma S_1^2}{2S_3 S_2^3} \tag{7.15}$$

$$\|\nabla \times n \times n\|^2 = \frac{1}{\beta^2}\left(\frac{S_1^2 S_3 - 2\tau S_2}{S_1^2 S_2^2 S_3} + \frac{\sigma^2(S_2^2 + S_3^2 - S_1^2\cos(2(\beta q\sigma + u)))^2}{4S_2^6 S_3^2}\right) \tag{7.16}$$

We want to adimensionalize the previous quantities, to decrease the number of variables. Since the former have to be integrated on a set of fixed volume V, we use $V^{1/3}$ as length to rescale the coordinates. The length scale of the spheroidal coordinates is given by β therefore it becomes

$$\beta \to \beta V^{1/3} \tag{7.17}$$

another length scale is given by the pitch of the nematic field, through $q = 2\pi/p$

$$p \to p V^{1/3} \Rightarrow q \to q/V^{1/3} \tag{7.18}$$

From the energy densities showed in the previous section, we get that the bend and splay characteristic length is given by β, while the twist scales both with q and β.

7.5 The droplet shape

In the following we will integrate the Frank-Oseen energy in an ellipsoid, with its axis directed along e_z, with aspect ratio α and volume V. Since the volume

is simply given by

$$V = \frac{4}{3}\pi\alpha r^3 \tag{7.19}$$

where r is the radius, we get that the domain of integration can be expressed as follows

$$x^2 + y^2 + \frac{z^2}{\alpha^2} \leq r^2 = \left(\frac{3}{4\pi\alpha}\right)^{2/3} V^{2/3} \tag{7.20}$$

therefore by scaling the coordinates by a factor $V^{1/3}$, $x \to x\, V^{1/3}$ we get

$$x^2 + y^2 + \frac{z^2}{\alpha^2} \leq \left(\frac{3}{4\pi\alpha}\right)^{2/3} \tag{7.21}$$

which is independent of the volume V.

7.6 Twist energy

For cholesterics we know that the twist energy density f_2 is given by

$$f_2 = (\nabla \times n \cdot n - q_\infty)^2 \tag{7.22}$$

that can be expanded into three terms

$$f_2 = (\nabla \times n \cdot n)^2 - 2q_\infty (\nabla \times n \cdot n) + q_\infty^2; \tag{7.23}$$

As shown in (7.15), the $\nabla \times n \cdot n$ has two parts, one scaling with q and one with $1/\beta$. We define $t_{11} := S_3/S_2$ and $t_{10} := \sin(2(\beta q \sigma + u))\sigma S_1^2/2S_3 S_2^3$ so that (7.15) $= q t_{11} + t_{10}/\beta$, and (7.23) becomes

$$f_2 = q^2 t_{22} + \frac{q}{\beta} t_{21} + \frac{1}{\beta^2} t_{20} - 2q_\infty \left(q\, t_{11} + \frac{1}{\beta} t_{10}\right) + q_\infty^2 \tag{7.24}$$

where $t_{22} := t_{11}^2$, $t_{21} := 2t_{11}t_{10}$ and $t_{20} := t_{10}^2$. Integrating f_2 over the ellipse of (7.21) we get

$$F_2 = \int f_2 \, dV = q^2 T_{22} + \frac{q}{\beta} T_{21} + \frac{1}{\beta^2} T_{20} - 2q_\infty \left(q\, T_{11} + \frac{1}{\beta} T_{10}\right) + q_\infty^2 \tag{7.25}$$

where the uppercase T_{ij} is the integral over the volume of the respective t_{ij} and depends on q, β and α.

Since the volume of integration is set to be 1, we can go back to $q \to V^{-1/3}q$ to get the energy for each V, while we keep β adimensional.

$$F_2 = V \int f_2 \, dV = q^2 V T_{22} + V^{2/3} \frac{q}{\beta} T_{21} + \frac{V^{1/3}}{\beta^2} T_{20} - 2q_\infty \left(q\, T_{11} V + \frac{1}{\beta} T_{10} V^{2/3}\right) + q_\infty^2 V \tag{7.26}$$

We can regroup the terms depending on V to obtain

$$F_2 = V(q^2 T_{22} - 2q_\infty q T_{11} + q_\infty^2) + \frac{V^{2/3}}{\beta}(q T_{21} - 2q_\infty T_{10}) + \frac{V^{1/3}}{\beta^2}T_{20} \quad (7.27)$$

Looking closely at t_{10}, we notice that its dependence on u is only in the form

$$t_{10} \propto \sin(2u + ...) \quad (7.28)$$

If we parametrize the domain of integration, the ellipsoid, with cylindrical coordinates around the x axis,

$$\begin{aligned} x &= x \\ y &= \rho \cos u \\ z &= \rho \sin u \end{aligned} \quad (7.29)$$

the domain of integration for u will be of the form $[\pi/2 - \delta, \pi/2 + \delta]$ and $[-\pi/2 + \delta, -\pi/2 - \delta]$, where δ depends only on x and ρ. Therefore the integral on these domains of (7.28) is zero, and $T_{10} = 0$.

The same can be done for T_{21} since t_{11} does not depend on u, and both terms for symmetry are zero. The twist energy has the form

$$F_2 = K_2 V(q^2 T_{22} - 2q_\infty q T_{11} + q_\infty^2) + K_2 \frac{V^{1/3}}{\beta^2}T_{20} \quad (7.30)$$

7.7 Bulk energy

Both bend and splay energy density depend on the product $q\beta$ and are inversely proportional to β^2. Let F_1 be the splay energy and F_3 the bend energy. We define Y and B to simplify the notation as the quantities satisfying

$$F_1 := K_1 \frac{V^{1/3}}{\beta^2} Y \quad (7.31)$$

$$F_3 := K_2 \frac{V^{1/3}}{\beta^2} B \quad (7.32)$$

so together with (7.30) we get

$$\frac{F_B}{K_2} = \frac{V^{1/3}}{\beta^2}(\kappa_1 Y + \kappa_3 B + T_{20}) + V(q^2 T_{22} - 2q_\infty q T_{11} + q_\infty^2) \quad (7.33)$$

where $\kappa_1 := K_1/K_2$ and $\kappa_3 := K_3/K_2$.

7.8 Total energy

The surface energy term is given by

$$F_S = \gamma \int 1 + \omega(n \cdot \nu)^2 \, dS. \tag{7.34}$$

Changing coordinates such that $\beta \to \beta V^{1/3}$ we get

$$F_S = \gamma V^{2/3} \left(S + \omega A \right) \tag{7.35}$$

where S is the surface of the ellipsoid and depends solely on α, while A is the anchoring term and depends on α, β and $qV^{1/3}$. By putting everything together we get

$$F = K_2 V (q^2 T_{22} - 2q_\infty q T_{11} + q_\infty^2) + \gamma V^{2/3} \left(S + \omega A \right) + K_2 \frac{V^{1/3}}{\beta^2} \left(\kappa_1 Y + \kappa_3 B + T_{20} \right) \tag{7.36}$$

7.9 Numerical analysis

In order to minimize the energy (7.36), we need to set the values of the various parameter. In [15] and [2], they were estimated as:

$$
\begin{aligned}
K_2 &= 0.3 \cdot 10^{-5} \mu N & \kappa_1 &= 3 & \kappa_3 &= 3 \\
\gamma &= 0.6 \cdot 10^{-6} N m^{-1} & \omega &= 2 & & \\
q_\infty &= 0.4 \, \mu m^{-1} & p_\infty &= 15 \, \mu m &
\end{aligned}
\tag{7.37}
$$

However to better fit the data, both $\kappa_{1,3}$ and γ have been adapted by a factor 2, that is

$$\gamma = 1.2 \cdot 10^{-6} N m^{-1} \qquad \kappa_1 = \kappa_3 = 6 \tag{7.38}$$

The comparison with the experimental data will be discussed in the last section. We use q, β and α as the parameters to minimize the free energy, while we change the volume from $V = 10 \, (\mu m)^3$ to $V = 10^6 \, (\mu m)^3$. We span β from 0.05 to 2 with steps of 0.05 and q from 0 to 40 with steps of 0.1. The last parameter is α and it goes from 0.75 to 3.0 with steps of 0.25. Each integral is calculated with a step of 0.004, in an ellipse of volume 1, and finally rescaled by V.

In Figure 7.4 we show the plot of the parameters that minimize F, to improve the readability we divide β by the major axis of the ellipsoid that is $\tilde{\beta} = \frac{\beta}{\left(\frac{3\alpha^2}{4\pi} \right)^{1/3}}$, so that when $\beta = 1$ we know that the foci of the director field lie on the vertices of the ellipsoid, for $\tilde{\beta} > 1$ they are outside and for $\tilde{\beta} < 1$ they are inside; on the other hand, instead of the twist number q, we plot the pitch $p = 2\pi/q$, that is a length, in micrometers.
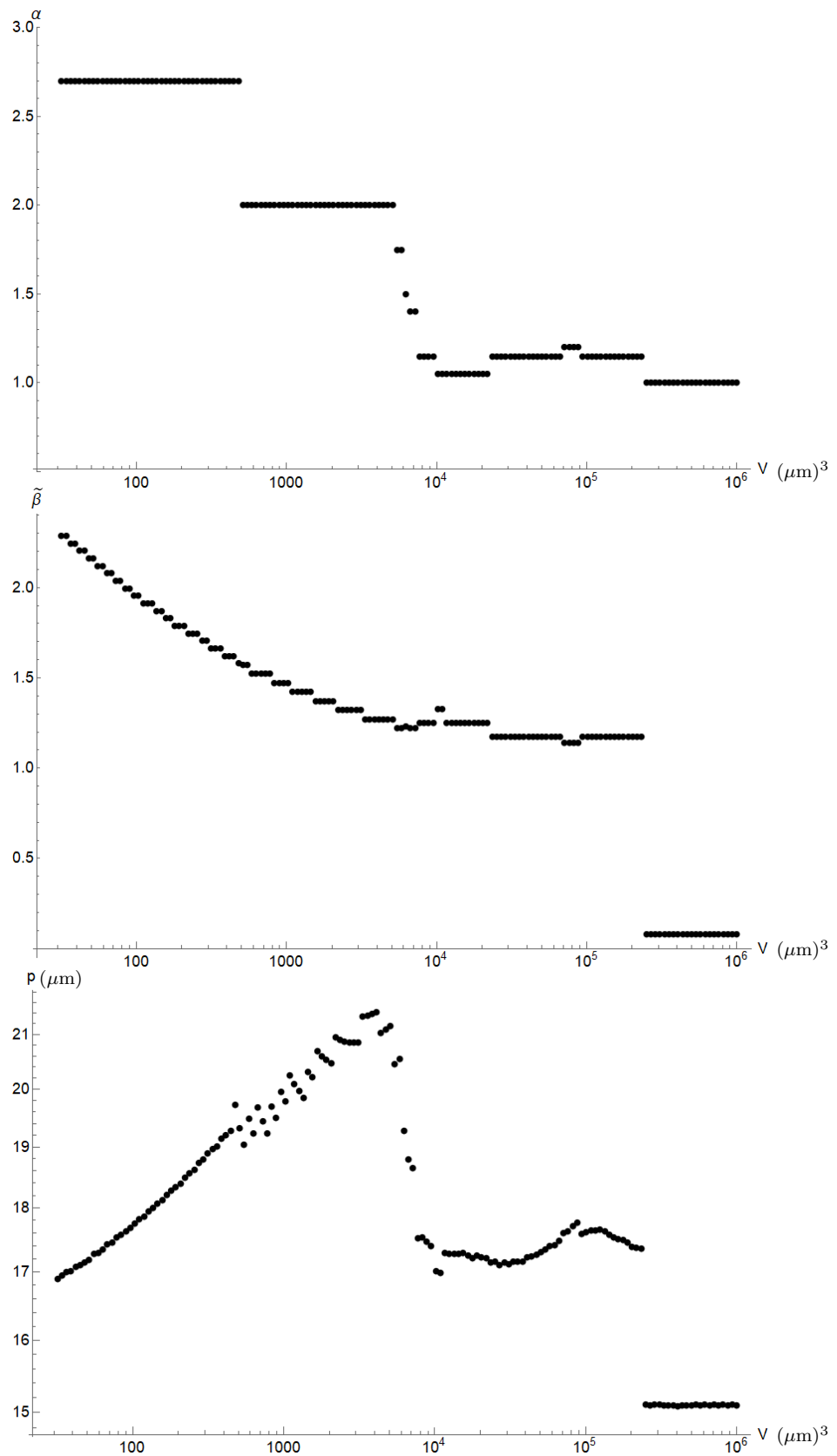
Figure 7.4: From top to bottom: Plot of the aspect ratio, plot of the parameter $\tilde{\beta}$ and plot of the pitch as a function of the volume V.
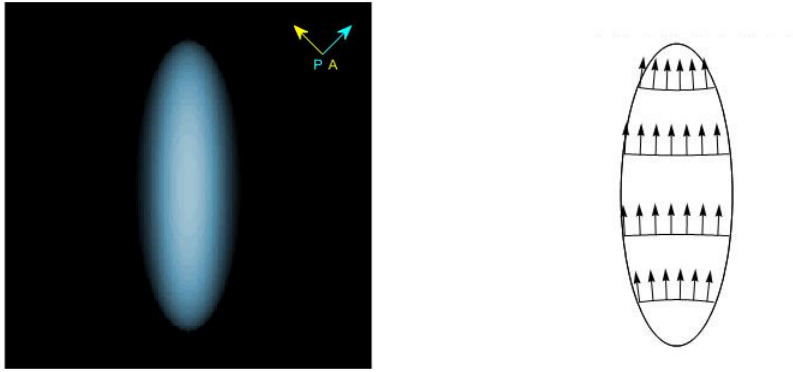
Figure 7.5: Jones' matrices simulation for $V = 100$, $\alpha = 2.7$, $\beta = 2$, and schematic of the director field

When the volume is very small, $V < 300(\mu m)^3$, the aspect ratio is quite high ($\alpha = 2.7$) , β is higher than 1 and decreasing with volume, the pitch is bigger than the size of the droplet, i.e. the nematic field is basically untwisted.

Therefore, for small volumes we obtain homogeneous droplets, as can be seen from the Jones matrix simulation in Figure 7.5.

As soon as the volume increases, β gets closer to one, and also the aspect ratio α decreases. This regime corresponds to the continuous transition from a homogeneous droplet, $\beta \gg 1$, to a bipolar one, $\beta \sim 1$. This transition has been better explained by [36], and in the previous chapter. As soon as the volume reaches a value of $1000(\mu m)^3$ the typical signs of the bipolar droplets appear, as shown in Figure 7.6.

Figure 7.6: Jones matrices simulation for $V = 1000$, $\alpha = 2.5$, $\beta = 1.2$. At two different angles of the polarizers.

In this model the shape is an ellipsoid with only α as a degree of freedom. Since this transition is mainly led by the anchoring energy, and the anchoring is strongly dependent on the shape of the droplet, the results for the homogeneous to bipolar droplet show some noise due to numerical imprecision.

When the volume reaches $\sim 3000 \mu m^3$, the pitch goes from increasing to sharply decreasing. We are in the region where $V^{1/3}$ is in the same order of magnitude of the pitch. From $V > 3000 \mu m^3$ we observe a constant aspect ratio $\alpha = 1.15$ and a slowly decreasing β.
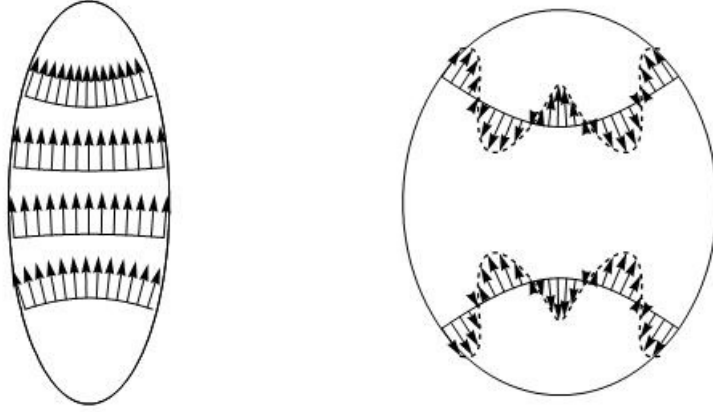
Figure 7.7: Schematics of the nematic field in case of a bipolar droplet $\beta = 1.5$ and $\alpha = 2.5$, and for a cholesteric one $\beta = 1.2$, $\alpha = 1.15$.

We are in the regime of the cholesterics droplets. The higher the volume, the more bands we can see. The distance between bands is fixed at $p = 17 \mu m$, but different from the value of the natural pitch $p_\infty = 15 \mu m$. The Jones' matrices simulation are shown in Figure 7.8.

Differently from what is observed experimentally, here we see a constant pitch for increasing volume. This could be due to the shape of the droplet, since the anchoring strength is still important at these volumes. Increasing the degrees of freedom of the shape of the droplet may be a lead for further analysis.

As the volume of the particle is allowed to grow even further, $V > 3 \cdot 10^5 \mu m^3$, we see a sharp transition where β drops to zero, $p = p_\infty = 15 \mu m$ and $\alpha = 1$. This is the last transition observed experimentally. What the model predicts is the cholesteric to onion transition. We see that the pitch goes to its natural value, and the shape becomes a perfect sphere $\alpha = 1$. The value of $\beta = 0.05$ is the lowest value that it can assume numerically. Therefore it is legit to think that β may indeed tend to 0.
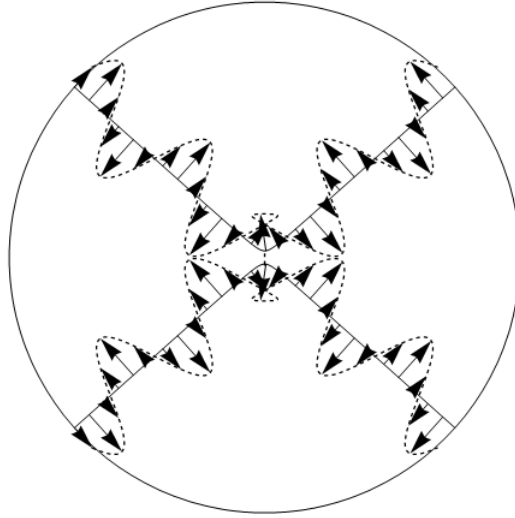
7.10   The onions

In the following we analyse each term in equation (7.36). The term T_{22} depends only on β and α. In the limit $\beta \to \infty$ and $\beta \to 0$, T_{22} tends to 1. For intermediate β, it presents a maximum depending on α.

Also T_{11} depends only on β and α, from Figure 7.11(b) we get the same behaviour as T_{22}.
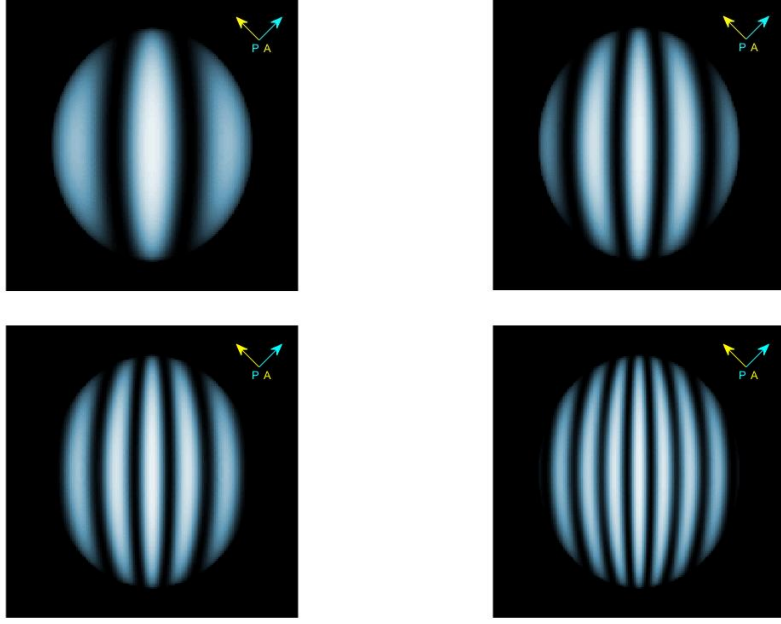
Figure 7.8: Jones' matrices simulation for $\alpha = 1.15$, $\beta = 1.2$ and $V = 10^4, 5 \cdot 10^4, 10^5, 3 \cdot 10^5$.

Figure 7.9: Schematics of the nematic field in case of $\beta = 0.05$, $\alpha = 1$ and $q = q_\infty$.

From these two terms we can obtain the minimum q that minimizes the first term in (7.27). It corresponds to the minimum in case of $V \to \infty$.

$$\frac{dF_2}{dq} \overset{!}{=} 0 \Rightarrow q = \frac{T_{11}}{T_{22}} q_\infty, \tag{7.39}$$

or also

$$p = \frac{T_{22}}{T_{11}} p_\infty. \tag{7.40}$$
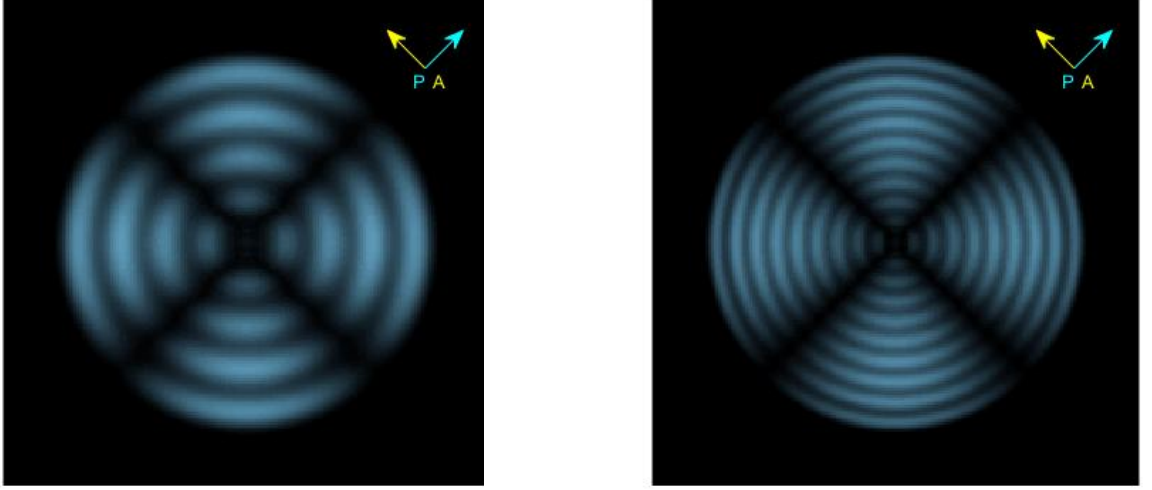
Figure 7.10: Jones' matrixes simulation for $\alpha = 1.$, $\beta = 0.05$ and $V = 3 \cdot 10^5, 10^6$.
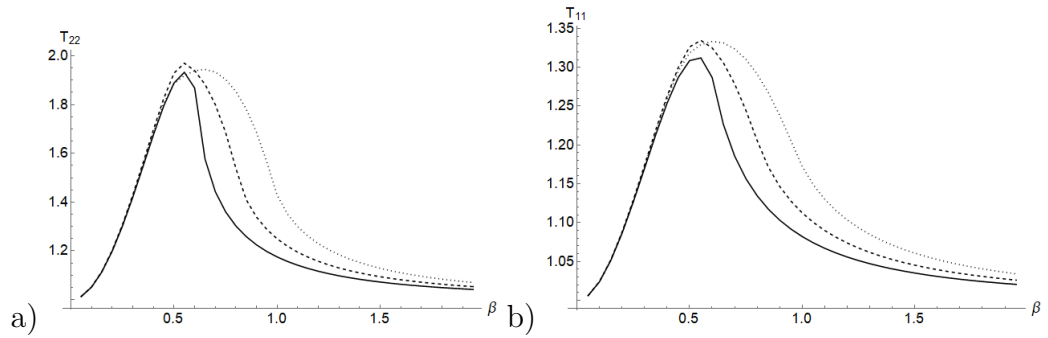

a)   b)

Figure 7.11: Plot of T_{22}(a) and T_{11}(b) versus β for $\alpha = 1$(solid), 1.5 (dashed), 2 (dotted).

The ratio T_{11}/T_{22} is plotted in Figure 7.12(a).
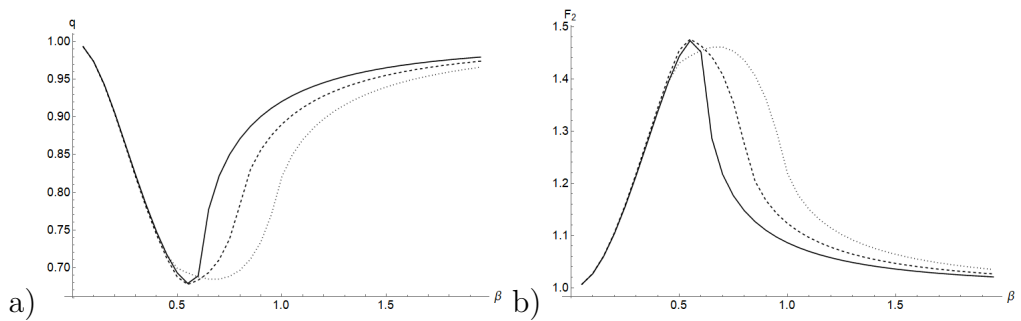

a)   b)

Figure 7.12: Plot of T_{22}/T_{11}(a) and F_2 at $q = T_{11}/T_{22}$(b) versus β for $\alpha = 1$(solid), 1.5 (dashed), 2 (dotted).

Calculating the energy at $q = \frac{T_{11}}{T_{22}} q_\infty$ we get

$$F_2 = V q_\infty^2 \left(1 - \frac{T_{11}}{T_{22}} \right), \qquad (7.41)$$

therefore in the limit $V \to \infty$, from Figure 7.12(b) we get that either $\beta \to \infty$ or $\beta \to 0$. We notice that is true for every value of α considered.

Next we analyze the second term given by

$$\gamma V^{2/3} \left(S + \omega A \right). \tag{7.42}$$

The anchoring depends only on the product $\beta q V^{1/3}$. When the twist is minimized, $q = q_\infty$, and $\beta = 0$ or $\beta = \infty$. In the case $\beta = 0$, the anchoring depends on α as in Figure 7.13(a). In case of $\beta \to \infty$, from the previous chapter, we
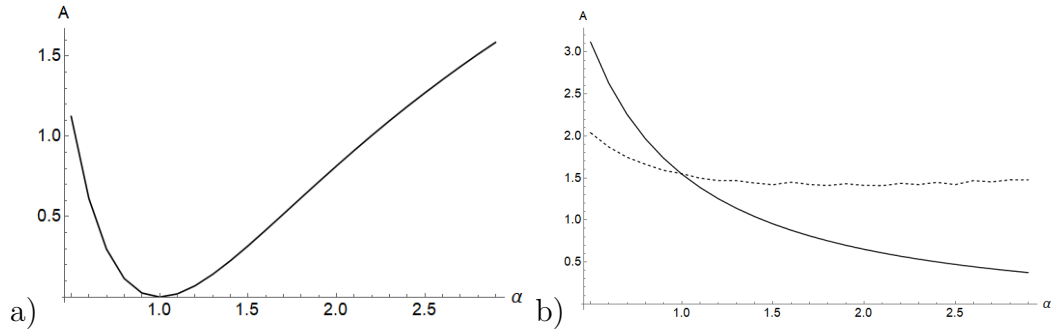
Figure 7.13: (a) Plot of A for $\beta = 0$ against α; (b) Plot of A for $\beta \to \infty$ against α for $\beta q_\infty V^{1/3} \to 0$ (solid) and $\beta q_\infty V^{1/3} \to \infty$ (dashed).

have basically two possible regimes $\beta q_\infty V^{1/3} \to 0$, in Figure 7.13(b, solid), and $\beta q_\infty V^{1/3} \to \infty$, in Figure 7.13(b, dashed). We know that S depends only on α and it reaches its minimum at $\alpha = 1$, therefore it is easy to see that in case of $V^{1/3} \to \infty$, we have

$$\beta = 0, \qquad q = q_\infty, \qquad \alpha = 1. \tag{7.43}$$

for whatever values of the parameters $K_i, \gamma, \omega (> 0)$.

However, when $\beta \to 0$ the $V^{1/3}$ term tends to infinity. In Figure 7.14 we plot the remaining three terms for $\alpha = 1$. They are

$$\frac{1}{\beta^2} \left(K_1 Y + K_3 B + K_2 T_{20} \right) \tag{7.44}$$

In the plot in Figure 7.14 we can see the behaviour of the three integrals, namely: B/β^2 (bend), Y/β^2 (splay) and T_{20}/β^2 (twist), expressed as a function of β. From the plot we see that the diverging term is given by the bend energy. Once we set $\alpha = 1$, to determine the equilibrium parameter of the onion we basically need three terms

$$V K_2 T q_\infty^2 + V^{2/3} \gamma \omega A + V^{1/3} K_3 \frac{B}{\beta^2} \tag{7.45}$$

where $T := \left(1 - \frac{T_{11}}{T_{22}} \right)$, as in equation (7.41).

By summing the above energies with the coefficients in (7.37) we get the behaviour for different volumes, shown in Figure 7.16.
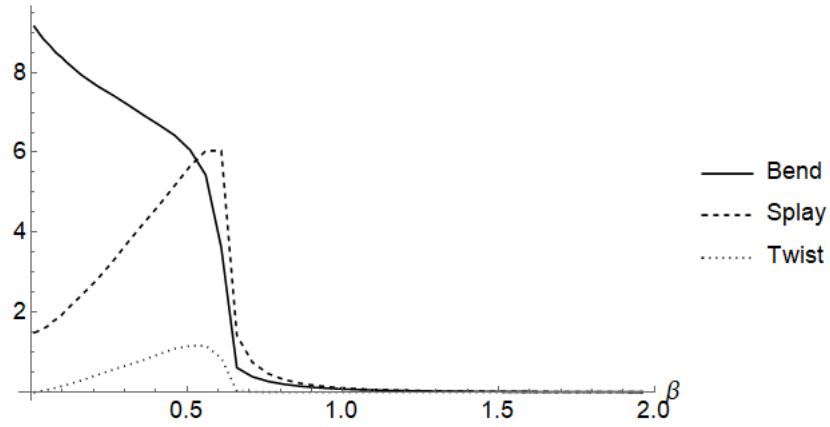
Figure 7.14: Plot of the $V^{1/3}$ terms: bend (solid), splay (dashed) and twist(dotted).
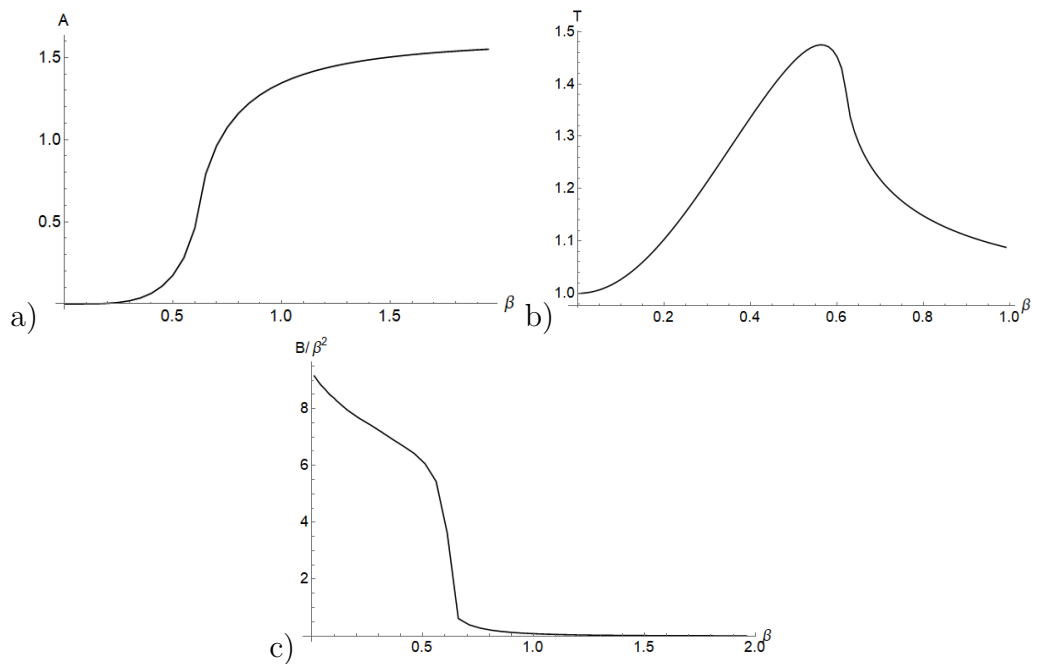
Figure 7.15: a)Plot of the anchoring energy A for $\alpha = 0$, as a function of β, for $q_\infty V^{1/3} \to \infty$. (b) Plot of the twist term T. (c) Plot of the bend term B/β^2.

Figure 7.16: Equation (7.45) for two different volumes $V = 10^4$ and 10^6.

The graphs show that the bend and the twist terms contribute to get the equilibrium value for β, while the anchoring decides whether we are in the

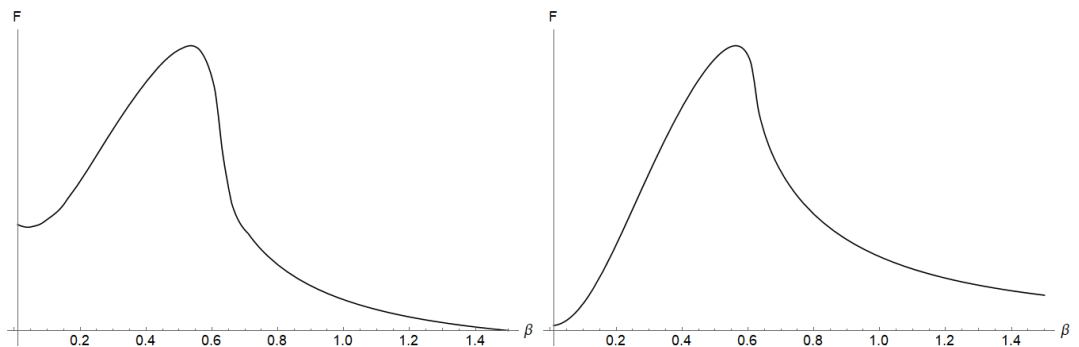cholesteric regime $\beta > 1$ or in the onion phase $\beta \to 0$. These plots only show qualitatively the transition between cholesteric and onion phase. In the following section we tackle the issue by a scaling approach.

7.11 A scaling approach

Guided by the previous section, we want to get a scaling relationship for the cholesterics-onion transition.

Looking at Figure 7.17 we know that β sets the scale of the inner core of the onion droplet, where basically the helixes (represented in dashed lines) of the cholesterics are untwisted. The outer shell of the onion contributes to the
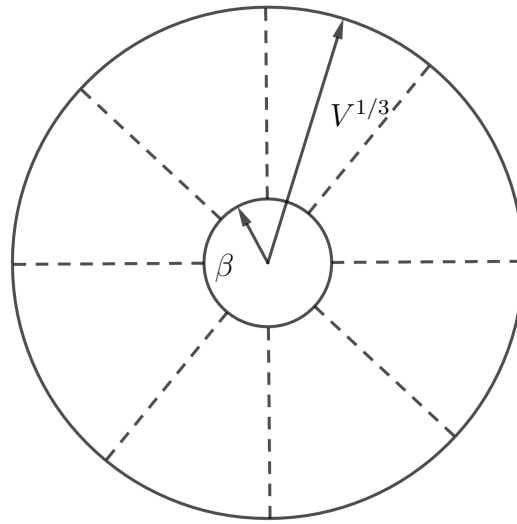
Figure 7.17: Schematics of a onion droplet, where the major radius scales with $V^{1/3}$ the inner radius scales with β. The cholesterics axes are drawn with a dashed line.

energy through the bend energy, whose energy density scales with $1/r^2$ that averaged on the shell gives:

$$\left\langle \frac{1}{r^2} \right\rangle = \frac{\int_{\beta}^{V^{1/3}} \frac{r^2}{r^2} dr d\theta d\phi}{V - \beta^3} \sim \frac{V^{1/3} - \beta}{V - \beta^3}. \tag{7.46}$$

Therefore the bend energy scales as

$$K_3(V - \beta^3) \left\langle \frac{1}{r^2} \right\rangle = K_3(V^{1/3} - \beta) \tag{7.47}$$

The inner core has an energy corresponding to the untwisted cholesterics is proportional to $K_2 \frac{V_{core}}{p_\infty^2}$. As the volume of the core is proportional β^3, we can write

$$F \sim K_3(V^{1/3} - \beta) + K_2 \frac{\beta^3}{p_\infty^2} \tag{7.48}$$

minimizing the former with respect to β we get

$$\beta \sim \sqrt{\frac{K_3}{K_2}} p_\infty = \sqrt{\kappa_3} p_\infty \tag{7.49}$$

Therefore the nucleus of the onion droplet has a radius that scales with p_∞. Putting back β into (7.48) we get

$$F_{onion} \sim K_3 \sqrt{\kappa_3} p_\infty \tag{7.50}$$

since at the minimum both terms have roughly the same intensity $(V^{1/3} - p_\infty) \sim p_\infty$.

A more general result can be obtained by considering an ellipse of aspect ratio α. In this case we set r and R as the minor and major axes, respectively, such that $R/r = \alpha$ and $V = \alpha r^3$. Following [3], the bending energy density scales as $(r/R^2)^2$. The average of that quantity on the outer shell becomes

$$\left\langle \frac{r^2}{R^4} \right\rangle = \left\langle \frac{1}{\alpha^4 r^2} \right\rangle = \frac{1}{\alpha^3} \frac{\int_\beta^{(V/\alpha)^{1/3}} dr d\theta d\phi}{V - \alpha\beta^3} = \frac{1}{\alpha^3} \frac{(V/\alpha)^{1/3} - \beta}{V - \alpha\beta^3} \tag{7.51}$$

In this case we have to consider the surface energy F_S. While we do not consider anchoring, under the hypothesis that the director field is always tangent to the surface.

A good approximation for the surface of an ellipsoid of aspect ratio α and volume V is

$$S \sim V^{2/3} \left(\frac{\left(1 + 2\alpha^{1.6}\right)^{1/1.6}}{\alpha^{2/3}} \right) \tag{7.52}$$

The total energy has the form

$$F = K \frac{\left(\frac{V}{\alpha}\right)^{1/3} - \beta}{\alpha^3} + K \frac{\alpha\beta^3}{p_\infty^2} + \gamma V^{2/3} \left(\frac{\left(1 + 2\alpha^{1.6}\right)^{1/1.6}}{\alpha^{2/3}} \right). \tag{7.53}$$

Minimizing with respect to β we obtain

$$\beta \sim \frac{p_\infty}{\alpha^2}, \tag{7.54}$$

and by the same argument as before we can simplify F as

$$F \propto K \frac{p_\infty}{\alpha^5} + \gamma V^{2/3} \left(\frac{\left(1 + 2\alpha^{1.6}\right)^{1/1.6}}{\alpha^{2/3}} \right). \tag{7.55}$$

For large volumes $V \gg \left(\frac{Kp_\infty}{\gamma}\right)^{3/2}$ the surface term prevails. As expected $\alpha \to 1$, and we get the results obtained in (7.50).

To get the transition from the uniaxial cholesteric, we want to compare this energy with the anchoring energy of the cholesterics droplet:

$$F_{chol} \sim \gamma \omega V^{2/3} \tag{7.56}$$

If we set them equal we get the critical volume

$$V_{c \to o} \sim \left(\frac{K_3\sqrt{\kappa_3}p_\infty}{\gamma\omega}\right)^{3/2} \tag{7.57}$$

or in case of single constant approximation where $\kappa_3 = 1$ and $K_3 = K$ we get

$$V_{c \to o} \sim \left(\frac{Kp_\infty}{\gamma\omega}\right)^{3/2} \tag{7.58}$$

From equation (7.49) we expect β to be constant in the onion regime, while for adimensional $\beta \to \beta V^{1/3}$,

$$\beta \sim \sqrt{\kappa_3}\frac{p_\infty}{V^{1/3}}. \tag{7.59}$$

decreases with $V^{-1/3}$. In our case where $\kappa_3 = 6$ and $V \sim 10^6$, gives $\beta \sim 0.3$. In the numerical model described above, we get a value of $\beta = 0.05$, which is 6 times lower than the the value expected with the scaling approach.

From [15], the radius of the onion's core was measured to be $\beta = p_\infty/2 = 7.5\mu$m, and constant with volume. Therefore the scaling correctly predicts the behaviour.

The numerical model correctly predicts the transition volume but is not sufficient to describe the core. This may be due to the integration precision, because the closer β gets to zero, the less precision is used to integrate the core.
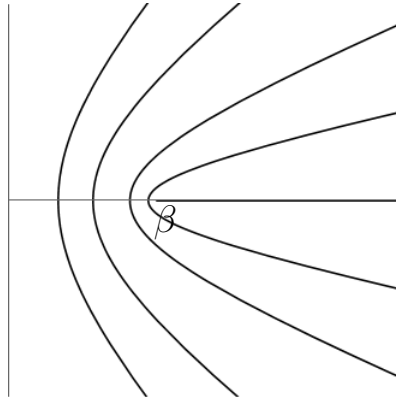
Figure 7.18: Magnification of the cholesteric axes in the neighbourhood of β.

The last reason could be that in the model the bending contributes also in the region inside the core, see Figure 7.18. On the other hand, in the scaling that part of the sphere is considered without bend and untwisted ($q = 0$).

7.12   Comparison with experimental data

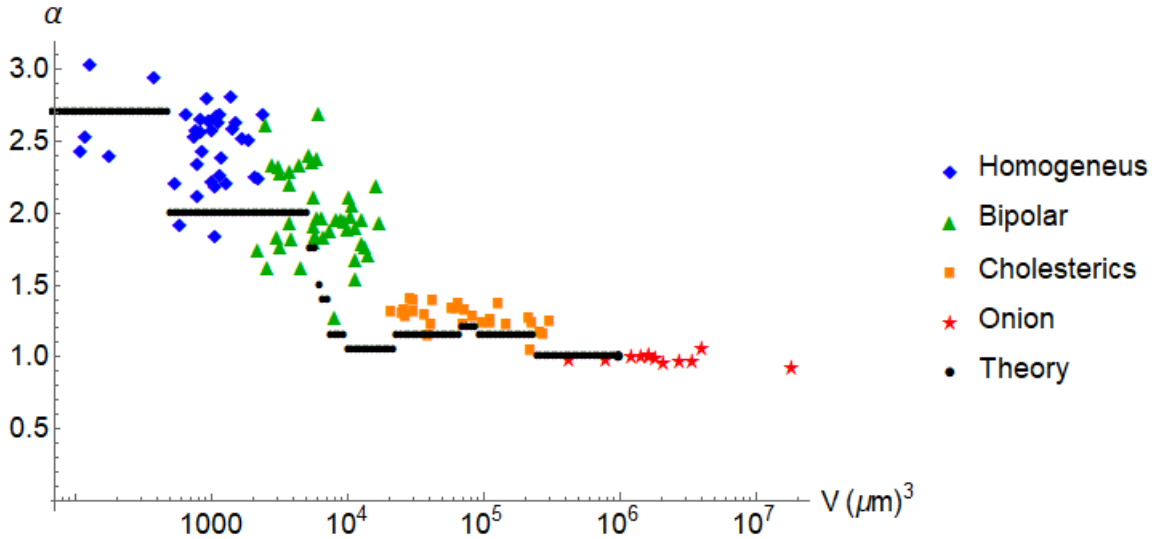In this section, we compare the results obtained with the numerical analysis, with the data from [15].

Figure 7.19: Measured aspect ratio plotted with theorical prediction.

In the graph in Figure 7.19, we see that the model successfully predicts the aspect ratio with a good approximation. For homogeneous and bipolar droplets, the aspect ratio is a continuously decreasing function of the volume, while the model predicts a stepwise behavior. In the cholesteric phase we get a slight lower aspect ratio $\alpha = 1.15$ than the measured $\alpha = 1.3$.

The transitions volumes are in good agreement with experiments, once parameters such as the ratio κ_3 and γ are suitably modified starting from the measured ones [2] to better fit these values.

The second set of data, shown in Figure 7.20, is given by the pitch of cholesteric and onion droplets.

The model completely misses to predict the correct value of the pitch, for cholesterics. While the pitch in the data decreases from almost $2p_\infty$ to p_∞, from the theory we get only a $+15\%$ increase.

In the cholesteric phase, as shown in Chapter 6, the major contribution to the free energy is given by anchoring. The anchoring energy depends on the angle between the nematic field and the normal to the surface, therefore contrary to the bulk energy, the shape of the surface influences strongly this term. The
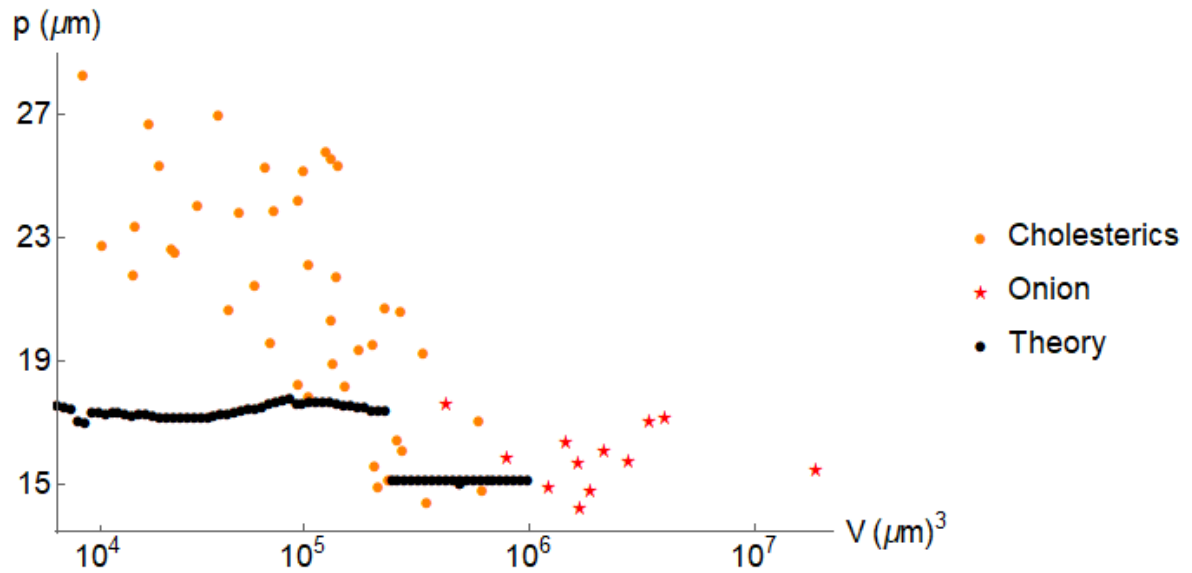
Figure 7.20: Measured pitch plotted with theorical prediction.

approximation, used to model the surface, is an ellipse with α, the aspect ratio, as the unique degree of freedom. For example, extending the analysis to a shape given by the elliptic lemon surface Chapter 4 is expected to have a strong impact on the results.

8. Conclusion and future perspectives

In this work, we addressed theoretically the effects of confinement on chiral liquid crystals. The theoretical models developed are based on the experimental works [2] and [15] of cholesteric droplets based on amyloid fibrils. The system, described in Chapter 2, shows four different phases for the droplets called, respectively: homogeneous, bipolar, cholesteric and onion.

The first model, presented in Chapter 5, focuses on the transition between the first two phases: the homogeneous to bipolar transition. It is able to fit the experimental data and through it we estimate a value of $\omega = 1.7$, very close to the previous estimate (in [2]) of $\omega = 2$. The model gives an estimate of the ratio between the bend elastic constant and the surface tension of $K_3/\gamma = 1\mu$m.

The second model, Chapter 6, was used to study the effects of boundary on a pure twisted director field, and served as a basis to build the third model in Chapter 7. The last model captures the full spectrum of droplets found by experiments. With good approximation, the model reproduces both the aspect ratio and the transition volumes. This last model gives an estimate of $\omega = 2$ and of $K_3/\gamma = 15\mu$m. Lastly, in Chapter 7, we introduced a scaling law for the last transition: from cholesteric to onion droplets.

There is an important difference between the two estimates of $K_3/\gamma = 1\mu$m and $K_3/\gamma = 15\mu$m. The first comes from the homogeneous and bipolar droplets, in the hypothesis that there is no twist. The second estimate is given by adjusting the transition volumes. The transition volumes also depend on K_2 and q_∞, which are not included in the bipolar model. Thus, an error on the estimate of K_2 and q_∞ could propagate into the estimate of K_3/γ.

The result of this work shows that this model can be the basis for further study. As already proposed, may be worth including the tip angle together with the aspect ratio as parameters for the shape of the droplet. Furthermore, the saddle-splay term, which in our analysis has never been considered, could be included into the energy terms. This however introduces a further complication, as the value of K_{24} is not known.

Finally, we note that the present approach is very general. The model was used to rationalize data from an experimental system of amyloid fibrils. Indeed, the properties of the system are brought into the theory only through the elastic

moduli, surface tension and natural pitch. Therefore, the model could be used for any other system of chiral liquid crystal, such as *nanocellulose* [38], by suitably modifying those quantities.

Bibliography

[1] Abdus Salam. The role of chirality in the origin of life. *Journal of Molecular Evolution*, 1991.

[2] M. Arcari G. Nyström and R. Mezzenga. Confinement-induced liquid crystalline transitions in amyloid fibril cholesteric tactoids. *Nature nanotechnologies*, 2018.

[3] Peter Prinsen and Paul Van Der Schoot. Shape and director-field transformation of tactoids. *Phys. Rev. E*, 68, 2003.

[4] Pierre-Gilles de Gennes and Jacques Prost. The physics of liquid crystals (international series of monographs on physics). *Oxford University Press, USA*, 1995.

[5] S. Chandrasekhar. *Liquid Crystals*. Cambridge University Press.

[6] Georges Friedel. *Les états mésomorphes de la matière*, volume 9. 1922.

[7] Iam-Choon Khoo. *Liquid crystals: physical properties and nonlinear optical phenomena*, volume 64. John Wiley & Sons, 2007.

[8] Leighton R Feynman R and Sands M. *The Feynman Lectures on Physics*. Library of Congress Catalog, 1964.

[9] Michael J Stephen and Joseph P Straley. Physics of liquid crystals. *Reviews of Modern Physics*, 1974.

[10] Wikimedia Commons. Nematische phase schlierentextur, 2005.

[11] R. Clark Jones. A new calculus for the treatment of optical systemsi. description and discussion of the calculus. *J. Opt. Soc. Am.*, 31, 1941.

[12] Anthony Gerrard and James M Burch. *Introduction to matrix methods in optics*. Courier Corporation, 1975.

[13] A Lien. Extended jones matrix representation for the twisted nematic liquid-crystal display at oblique incidence. *Applied physics letters*, 57(26):2767–2769, 1990.

[14] Toralf Scharf. *Polarized light in liquid crystals and polymers*. John Wiley & Sons, 2007.

[15] G. Nyström M. Bagnani and R. Mezzenga. Amyloid fibrils length controls shape and structure of nematic and cholesteric tactoids. *unpublished article*, 2018.

[16] Yves Bouligand and Françoise Livolant. The organization of cholesteric spherulites. *Journal de Physique*, 45(12):1899–1923, 1984.

[17] Vida Jamali, Natnael Behabtu, Bohdan Senyuk, J Alex Lee, Ivan I Smalyukh, Paul van der Schoot, and Matteo Pasquali. Experimental realization of crossover in shape and director field of nematic tactoids. *Physical Review E*, 91(4):042507, 2015.

[18] R. D. Williams. Two transitions in tangentially anchored nematic droplets. *J. Phys. A*, 19, 1986.

[19] Yunfeng Li, Jeffrey Jun-Yan Suen, Elisabeth Prince, Egor M Larin, Anna Klinkova, Héloïse Thérien-Aubin, Shoujun Zhu, Bai Yang, Amr S Helmy, Oleg D Lavrentovich, et al. Colloidal cholesteric liquid crystal in spherical confinement. *Nature communications*, 7:12520, 2016.

[20] F. C. Frank. I. liquid crystals. on the theory of liquid crystals. *Discussions of the Faraday Society*, 25:19–28, 1958.

[21] Rapini, A. and Papoular, M. Distorsion d'une lamelle nématique sous champ magnétique conditions d'ancrage aux parois. *J. Phys. Colloques*, 1969.

[22] CW Oseen. The theory of liquid crystals. *Transactions of the Faraday Society*, 29(140):883–899, 1933.

[23] H Zocher. Spontaneous structure formation in sols; a new kind of anisotropic liquid media. *Z Anorg Allg Chem*, 147:91–110, 1925.

[24] Epifanio G Virga. *Variational theories for liquid crystals*, volume 8. CRC Press, 1995.

[25] James Nearing. *Mathematical tools for physics*. Dover Publications, 2017.

[26] Jürgen Nehring and Alfred Saupe. On the elastic theory of uniaxial liquid crystals. *The Journal of Chemical Physics*, 54(1):337–343, 1971.

[27] Zvetkov V. *Acta Phys. Chym*, 1937.

[28] GR Luckhurst, David A Dunmur, and Atsuo Fukuda. *Physical properties of liquid crystals: nematics*. Number 25. IET, 2001.

[29] Carl Wilhelm Oseen. Probleme für die theorie der anisotropen flüssigkeiten. *Zeitschrift für Kristallographie-Crystalline Materials*, 79(1-6):173–185, 1931.

[30] C-C Wang. A new representation theorem for isotropic functions: An answer to professor gf smith's criticism of my papers on representations for isotropic functions. *Archive for rational mechanics and analysis*, 36(3):166–197, 1970.

[31] D Rivière, Yves Levy, and E Guyon. Determination of anchoring energies from surface tilt angle measurements in a nematic liquid crystal. *Journal de Physique Lettres*, 40(10):215–218, 1979.

[32] D. Langevin and M. A. Bouchiat. Molecular order and surface tension for the nematic-isotropic interface of mbba, deduced from light reflectivity and light scattering measurements. *Molecular Crystals and Liquid Crystals*, 22(3-4):317–331, 1973.

[33] Georg Wulff. Xxv. zur frage der geschwindigkeit des wachsthums und der auflösung der krystallflächen. *Zeitschrift für Kristallographie-Crystalline Materials*, 34(1-6):449–530, 1901.

[34] S. Hildebrandt and A. Tromba. *Mathematics and optimal forms.* Scientific American Books, 1995.

[35] Eric W. Weisstein. *Lemon.* MathWorld–A Wolfram Web Resource.

[36] Peter Prinsen and Paul van der Schoot. Parity breaking in nematic tactoids. *Journal of Physics: Condensed Matter*, 16(49), 2004.

[37] Philip McCord Morse and Herman Feshbach. *Methods of theoretical physics.* Technology Press, 1946.

[38] Jan PF Lagerwall, Christina Schütz, Michaela Salajkova, JungHyun Noh, Ji Hyun Park, Giusy Scalia, and Lennart Bergström. Cellulose nanocrystal-based materials: from liquid crystal self-assembly and glass formation to multifunctional thin films. *NPG Asia Materials*, 2014.